BIOCHEMISTRY

A hotspot for posttranslational modifications on the androgen receptor dimer interface drives pathology and anti-androgen resistance

Andrea Alegre-Martí[1,2]†, Alba Jiménez-Panizo[1,2]†, Adrián Martínez-Tébar[3]†, Coralie Poulard[4], M. Núria Peralta-Moreno[5], Montserrat Abella[1,2], Rosa Antón[6], Marcos Chiñas[3,7], Ulrich Eckhard[8], Josep M. Piulats[3], Ana M. Rojas[9], Juan Fernández-Recio[10], Jaime Rubio-Martínez[5], Muriel Le Romancer[4], Álvaro Aytes[3]‡*, Pablo Fuentes-Prior[6]‡*, Eva Estébanez-Perpiñá[1,2]‡*

Mutations of the androgen receptor (AR) associated with prostate cancer and androgen insensitivity syndrome may profoundly influence its structure, protein interaction network, and binding to chromatin, resulting in altered transcription signatures and drug responses. Current structural information fails to explain the effect of pathological mutations on AR structure–function relationship. Here, we have thoroughly studied the effects of selected mutations that span the complete dimer interface of AR ligand–binding domain (AR-LBD) using x-ray crystallography in combination with in vitro, in silico, and cell-based assays. We show that these variants alter AR-dependent transcription and responses to anti-androgens by inducing a previously undescribed allosteric switch in the AR-LBD that increases exposure of a major methylation target, Arg[761]. We also corroborate the relevance of residues Arg[761] and Tyr[764] for AR dimerization and function. Together, our results reveal allosteric coupling of AR dimerization and posttranslational modifications as a disease mechanism with implications for precision medicine.

INTRODUCTION

The androgen receptor (AR; *AR/NR3C4*) is a member of the steroid subfamily of nuclear receptors essential for male development and tissue homeostasis (*1–2*). The AR protein is composed of an intrinsically disordered N-terminal region (NTD) followed by a "core" that contains the actual DNA- and ligand-binding domains (DBD and LBD, respectively) (Fig. 1A) (*2–3*). The atomic details of full-length AR (FL AR) still remain elusive, but a low-resolution structure by cryo–electron microscopy (cryo-EM) complexed to DNA and a coregulator has provided a model of its overall architecture (*4*). This EM structure features a noncanonical head-to-head dimer (i.e., centered on H5 helices, in contrast to the canonical, H10-centered arrangement [see (*3*) for a detailed comparison of the dimerization modes], in line with previously reported x-ray structures of dimeric DBD (*5*) and LBD isolated moieties (*6*).

Another EM structure of the AR core has recently been published in three distinctive configurations (*7*), further corroborating the noncanonical AR-LBD dimerization mode (*3*). These EM structures evidence that AR is a highly dynamic protein. AR physiological functions are inherently linked to not only the correct folding of DBD and LBD modules but also to their relative orientations (e.g., N-terminal and C-terminal (N/C) interaction), oligomerization, and coregulator binding to control transcription (*2, 8*). Besides, AR protein structure and function relationship are regulated by posttranslational modifications (PTMs) such as methylation, phosphorylation, ubiquitination, acetylation, and sumoylation, adding an extra level of complexity that has only been scarcely studied (*9–19*). In particular, no structural data have been reported on the mechanistic consequences of these covalent modifications to date.

Tight spatial and temporal regulation of AR activity is critical for the proper functioning of tissue-specific signaling cascades. Therefore, dysfunctions of the AR-regulated pathways have profound pathophysiological consequences (*2, 8, 20–22*). Up-regulated receptor activity is the dominant driver in one of the leading cancers in adult men, prostate cancer (PCa; *1–2, 8, 21–22*), making AR a central therapeutic target for PCa treatment (*2*). On the other hand, impaired response to androgens leads to an X chromosome–linked disorder of sex development in genetic males termed androgen insensitivity syndrome (AIS) (*23–25*). Many point mutations in the *AR* gene associated with either resistance to PCa therapeutic drugs (anti-androgens; *26–28*) and/or with AIS have been reported (*29*) (table S1 and Fig. 1A). Knowledge of the structure of the wild-type (WT) protein does not allow to predict the structural and functional impact of point mutations and therefore their pathogenicity and clinical implications in patients (*3, 6–7*). Whereas mutations causing AIS occur in the germ line, PCa-linked mutations are mostly somatic and occur before endocrine treatment or

[1]Structural Biology of Nuclear Receptors, Department of Biochemistry and Molecular Biomedicine, Faculty of Biology, University of Barcelona (UB), 08028 Barcelona, Spain. [2]Institute of Biomedicine of the University of Barcelona (IBUB), University of Barcelona (UB), 08028 Barcelona, Spain. [3]Programs of Molecular Mechanisms and Experimental Therapeutics in Oncology (ONCOBell) and Cancer Therapeutics Resistance (ProCURE), Catalan Institute of Oncology, Bellvitge Institute for Biomedical Research, 08908 Barcelona, Spain. [4]Cancer Research Center of Lyon, CNRS UMR5286, Inserm U1502, University of Lyon, 69000 Lyon, France. [5]Department of Materials Science and Physical Chemistry, Faculty of Chemistry and Institut de Recerca en Química Teorica i Computacional (IQTCUB), 08028 Barcelona, Spain. [6]Biomedical Research Institute Sant Pau (IIB Sant Pau), 08041 Barcelona, Spain. [7]Universidad Nacional Autónoma de México, Centro de Ciencias Genómicas, Cuernavaca, 61740 Morelos, Mexico. [8]Department of Structural and Molecular Biology, Molecular Biology Institute of Barcelona (IBMB-CSIC), 08028 Barcelona, Spain. [9]Computational Biology and Bioinformatics, Andalusian Center for Developmental Biology (CABD-CSIC), 41013 Sevilla, Spain. [10]Instituto de Ciencias de la Vid y del Vino (ICVV-CSIC), CSIC-UR-Gobierno de La Rioja, 26007 Logroño, Spain.
†These authors contributed equally to this work.
‡These authors contributed equally to this work.
*Corresponding author. Email: evaestebanez@ub.edu (E.E.-P.); fuentespriorpablo@gmail.com (P.F.-P.); aaytes@idibell.cat (A.A.)

Fig. 1. Mutations at the AR-LBD dimer interface affect cellular phenotypes, transcriptional activity, and response to antiandrogens. (**A**) Cartoon of AR domain organization. Physiologically relevant interaction sites [top; activation function-1 (AF-1), AF-2 and binding function-3 (BF-3)], mutated AR-LBD residues (red; middle), and secondary structure elements [bottom; helices (H, cylinders) and β strands (S1 to S4, triangles)] are indicated. Neighboring residues of major PTM sites are shown [methylation (M), phosphorylation (P), and ubiquitination (U)]. (**B**) Three-dimensional structure of AR-LBD (gray). Note that disease-linked residues (red spheres) and PTM sites (gray spheres) highlighted in (A) form an extended path on the AR-LBD dimer interface. (**C**) Relative AR transcriptional activity in CNT, WT, and mutant AR-transduced PC3 cells (mean ± SD, $n = 3$). Differences against WT were calculated using a t test and considered significant at P values <0.1. (#$P < 0.1$ *$P < 0.05$, **$P < 0.01$, ***$P < 0.001$, and ****$P < 0.0001$). The same P value guidelines and asterisk significance will be used through this manuscript. (**D**) Clonogenicity assay quantification in transduced PC3 cells (mean ± SD, $n = 3$). Representative crystal violet–stained cultures are shown in fig. S1A. (**E**) Time course of transduced PC3 cells proliferation (mean ± SD, $n = 3$). Proliferation is completely suppressed with WT AR or V785A but no other mutants. (**F**) Relative cell counts at day 7 after transduction. (**G** and **H**) Effect of anti-androgens on the relative AR transcriptional activity of transduced PC3 cells (mean ± SD, $n = 5$). (**I** and **J**) Viability fold change in response to anti-androgens in transduced cells relative to the CNT cells (mean ± SD, $n = 3$). Differences against CNT (D and F) between anti-androgen treated and nontreated cells (G and H) or against WT (I and J) were calculated using t tests. ns, not significant.
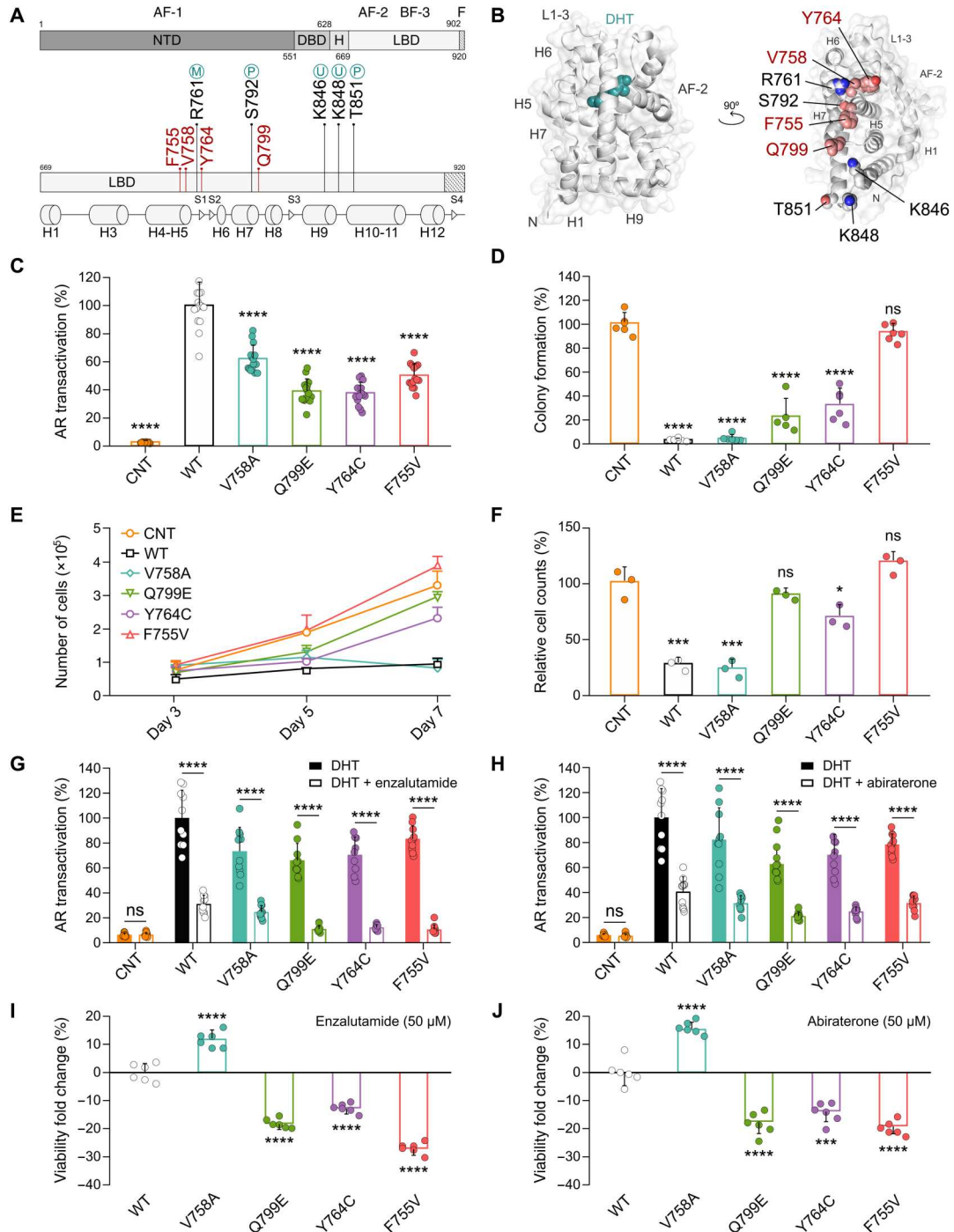
are induced by the selective pressure of anti-androgen therapies (2–3). While few mutations in PCa have been described as oncogenic or drivers (causative of the disease), most are considered passenger or silent mutations, although a contribution to PCa development and/or progression cannot be excluded (29–32).

To date, only three point mutants of the AR-LBD have been structurally characterized out of the over 350 reported variants (table S1). These oncogenic mutations (W742L, H875Y, and T878A) map to the internal ligand-binding pocket (LBP) and are responsible for rendering the anti-androgens cyproterone acetate, flutamide, and bicalutamide ineffective, respectively. Comparison of the WT AR-LBD and these mutant structures did not reveal any overall conformational changes. However, these mutations change the volume and shape of the LBP allowing the receptor to

remain active even in the presence of antagonists, thus explaining tumor escape from therapeutic control (2, 26–28). On the other hand, there are a wide variety of phenotypes associated with *AR* gene mutations in patient with AIS, ranging from mild symptoms (MAIS), to partial (PAIS) or completely feminized phenotypes (CAIS) (23–25, 33–34). Expectedly, about half of the CAIS-linked mutations map to the AR-LBD, but only a few of them can be easily rationalized as directly affecting hormone binding (3, 29).

AR-LBD pathogenic mutations outside the LBP may affect AR-dependent gene signatures through modulation of the monomer-oligomer equilibrium, accessibility of PTM sites, and/or by altering dynamic interactions with coregulators and chromatin. These processes are likely to be intricately intertwined and coupled via allosteric signaling transmission both within the AR monomer and across its dimerization interface (3–7). Here, we present a multidisciplinary investigation of the impact of several mutations of solvent-exposed AR-LBD residues identified in patients with PCa and/or AIS (Fig. 1A; see table S2 for major information on the studied mutations). Transcriptomic and in vitro cell–based assays demonstrate that these variants affect PCa proliferation and response to anti-androgens. Biochemical and biophysical investigations including high-resolution x-ray structures of mutant AR-LBD showed reduced thermal stability of the isolated domains as well as changes in the flexibility in functional sites of the receptor distal from the mutation site and unexpectedly revealed a previously unobserved rearrangement of the loop-featuring residue Arg[761]. The structural reorganization of this loop increases the degree of Arg[761] exposure, which correlated with an apparent increase in the extent of its methylation in cells. Together, our findings point to an intricate interplay between networks of local structural changes at and around the dimerization interface and global AR tertiary and quaternary structures that are coupled to PTM events. In turn, this network has a definite impact on AR transcriptional activity and gene programs that are affected by specific mutations. Our results may serve to predict the structural and functional impact of AR pathogenic mutations and open unexplored avenues for structure-guided modulation of its function in PCa tumors and patients with AIS.

RESULTS

We previously presented the crystal structure of the transcriptionally active, isolated dimeric AR-LBD (6) also corroborated in the multidomain protein (4, 7). The structural analysis revealed that the dimerization interface is a hotspot for mutations identified in patients with PCa and/or AIS [see (3) and table S1]. There was no clear-cut separation between PCa- and AIS-linked mutations, and some of these variants were linked to both conditions, albeit occurring in different developmental stages. These observations prompted us to perform a thorough characterization of the structural changes and functional impact of AR point mutants at the dimerization interface (Fig. 1B).

Mutations at the AR-LBD dimer interface differently affect cell proliferation and response to anti-androgens

To assess the functional impact of point mutations that affect the AR-LBD dimer interface, we generated AR-null PC3 cell lines (CNT) stably expressing either WT AR or mutants Phe[755]Val (F755V) (35–37), Val[758]Ala (V758A) (38–42), Tyr[764]Cys (Y764C)

(36, 39, 42–48), or Gln[799]Glu (Q799E) (39, 42, 44–45, 48–54) (Fig. 1, A and B). As expected, WT expression resulted in a 24.5-fold increase in AR transactivation as measured by luciferase reporter expression under the control of a synthetic AR promoter. All four mutants displayed a significantly lower AR transactivation activity compared to WT (Fig. 1C). Further, expression of WT and V758A resulted in a nearly complete inhibition of colony formation (Fig. 1D and fig. S1A) and proliferation (Fig. 1, E and F) compared to CNT cells that were highly statistically significant. Dihydrotestosterone (DHT) treatment of AR-transduced DU145 (fig. S2, B to D) and of AR-sensitive lymph node carcinoma of the prostate (LNCaP) cells (fig. S2, E to G) resulted in comparable growth-suppressive effects that were not observed in AR-negative parental DU145 cells (fig. S2, B to D), in a castration-resistant PCa cell line, 22rv1 (fig. S2, H to J), or in AR-insensitive, nontumor human prostate epithelial cells, RWPE1 (fig. S2, K to M). These observations confirm previous reports on the growth-suppressive effect of AR stimulation in AR-responsive cells (55, 56). In notable contrast, F755V and Q799E had proliferation rates not significantly different from those of the CNT cells, while proliferation was only modestly impaired by Y764C (Fig. 1, E and F). Similarly, colony forming capacity was unchanged for F755V and partially, albeit significantly, reduced in Glu[799]- and Cys[764]-expressing cells (Fig. 1D and fig. S1A).

Next, we asked whether the differences in proliferation and clonogenicity displayed by the AR variants would translate into distinct responses to anti-androgenic treatments. WT or mutant AR-expressing cells were treated with enzalutamide (Fig. 1, G and I), abiraterone (Fig. 1, H and J), or apalutamide (fig. S1B), and AR transactivation was measured. Transactivation was significantly inhibited by enzalutamide and abiraterone in both WT and mutant AR cells (Fig. 1, G and H). Reduction in AR transactivation was not a consequence of impaired cell viability upon anti-androgen treatment (Fig. 1, I and J, and fig. S1B). Specifically, V758A cells showed an 11.7, 20.6, and 16.1% increased viability compared to WT when treated with enzalutamide, apalutamide, or abiraterone, respectively. On the contrary, F755V, Y764C, and Q799E mutant cells displayed a significantly increased sensitivity to all three anti-androgens (Fig. 1, I and J, and fig. S1B).

Together, these results indicate that expression of ligand-bound WT AR in AR-null PCa cells induces a quiescent cell phenotype in AR-responsive cells without affecting the response to anti-androgen treatment. The data also demonstrate that, overall, point mutations at the AR dimerization surface negatively impact its ability to suppress proliferation and clonogenicity and mostly sensitize cells to anti-androgens (Fig. 1 and figs. S1, A and B, and S2).

Mutations at the AR-LBD dimer interface profoundly deregulate androgen-dependent transcription programs

Having demonstrated that dimerization surface mutations in the AR-LBD have an important impact on cellular functions, we next investigated whether these mutations alter gene expression patterns (Fig. 2 and fig. S1). Transcriptomic data were generated for WT and each mutant AR and compared to nontransduced cells as control. As expected, AR and canonical AR target genes such as *Transmembrane protease, serine 2* (*TMPRSS2*), *FK506-binding protein 5* (*FKBP5*), and *TCDD-inducible poly* [*ADP-ribose*] *polymerase* (*TIPARP*) were significantly up-regulated in both WT and mutant AR-expressing cells (Fig. 2A and fig. S1C), which was orthogonally

Fig. 2. The transcriptional profiles of AR-LBD dimerization surface mutants differ from that of the WT receptor. The results of RNA-seq experiments conducted in triplicate for each cell line are summarized. (**A**) Differential expression analysis between CNT and AR-transduced cells. Genes with |log$_2$(fold change)| ≥ 1 and P ≤ 0.05 are shown in red. (**B**) GSEA demonstrates similar signatures of WT and mutant AR. (**C**) Differentially expressed genes overlap between WT AR and its mutants. The bar plot (top) indicates the number of genes in the intersection between signatures. Vertical lines (bottom) connect the corresponding overlapping signatures. For each WT and mutant AR, signatures are separately given for up- (U) and down-regulated genes (D), and the size of the gene set is indicated (right). (**D** and **E**) Principal component analysis (PCA) and heatmap analysis of transcription profiles identifies three groups: (i) CNT, (ii) V785A and WT, and (iii) F755V, Y764C, and Q799E. (**F**) Volcano plots of AR target genes for WT and mutant AR. Canonical repressed (blue) and activated (red) AR targets are labeled. Note that repression of genes such as *MYC*, *SOX4*, *FOXA1*, and *CDH2* is lost in Q799E, Y764C, and F755V but not in V785A. (**G**) GSEA of the mutant AR signatures against WT AR on prostate cancer gene sets. Note that the V758A signature shows very limited overall enrichment indicating its strong similarity with WT. (**H**) GSEA of WT and mutant AR against a previously defined PCa malignancy signature (*58*). Enrichment for up- and down-regulated targets of the malignancy signature drivers *forkhead box protein M1* (*FOXM1*), *Centromere Protein F* (*CENPF*), or both are shown separately. Only the F755V, Y764C, and Q799E signatures are enriched in the *FOXM1* and/or *CENPF* regulons. Normalized enrichment score (NES) scale and false discovery rate (FDR) P value thresholds are indicated.
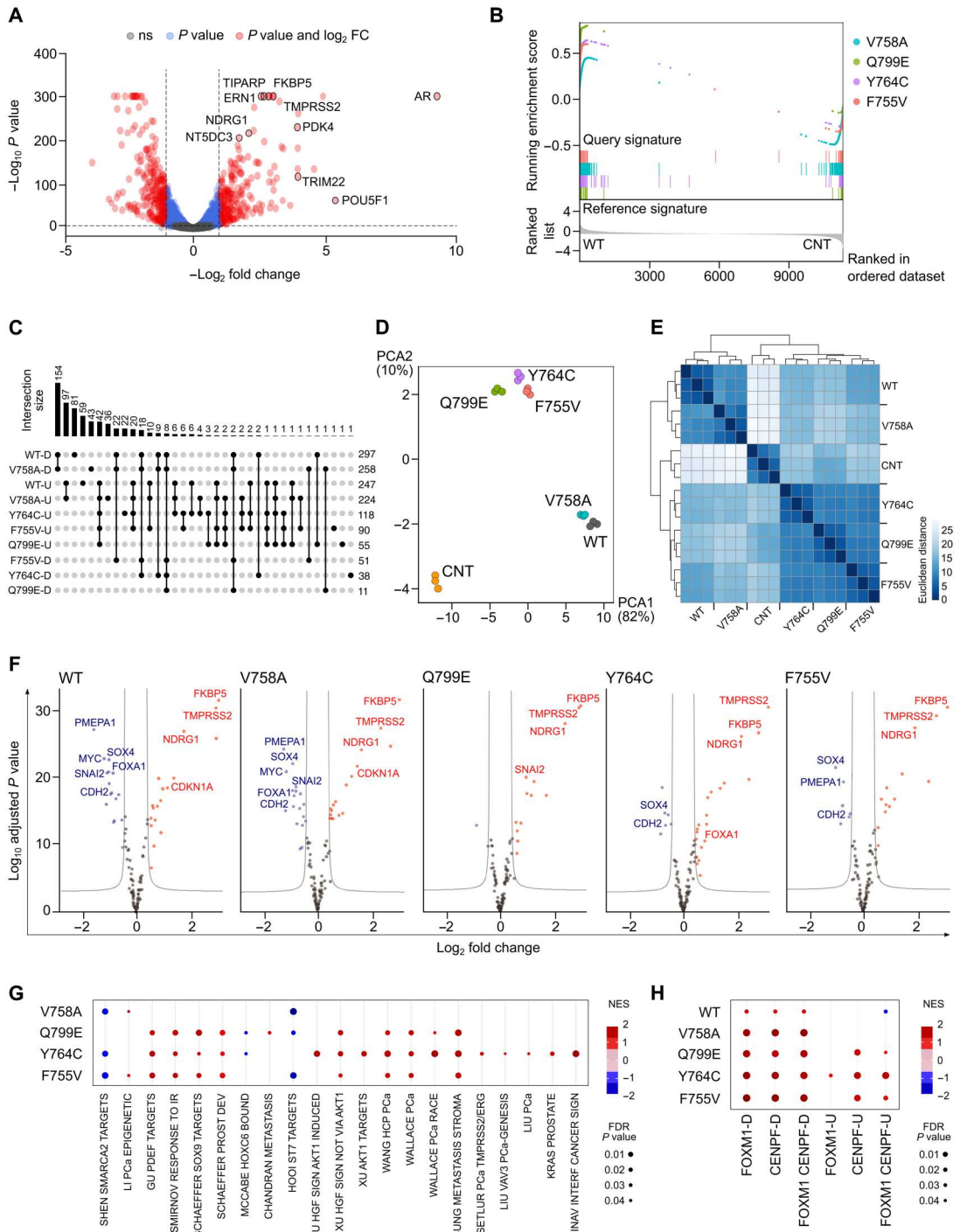
validated in quantitative polymerase chain reaction (qPCR) assays (fig. S1, G and H). In agreement with the functional evidence described above, the V758A mutant displayed AR target gene expression patterns most similar to WT AR (Fig. 2, C to E). Accordingly, gene set enrichment analysis (GSEA) showed that all four mutant AR signatures were similar to the WT signature (Fig. 2B). Although the AR regulon was conserved in all mutants, there were significant differences between the four variants. V758A showed a dynamic gene expression profile most similar to WT, while the differentially expressed gene (DEG) sets of F755V, Y764C, and Q799E were much smaller and shared fewer target genes compared to WT AR or V758A (Fig. 2C and fig. S1C). Variance assessment and clustering

of expression profiles further confirmed the similarity of WT and V758A transcriptomes, on the one hand, and those of F755V, Y764C, and Q799E, on the other. These two clusters were identified both by a principal components analysis (PCA) (Fig. 2D) and by clustering analysis computing sample-to-sample distances using variance-stabilizing transformation (VST) data (Fig. 2E). Further, gene expression in the AR regulon as defined by the DoRothEA collection of human regulons (57) showed that the set of activated AR target genes in WT and mutants remains largely conserved (Fig. 2F). However, only WT and V758A maintained a repressed gene set that included cancer drivers *Forkhead Box A1* (*FOXA1*) and *MYC proto-oncogen* (*MYC*) as well as epithelial-to-mesenchymal transition drivers *Snail Family Transcriptional Repressor 2* (*SNAI2/SLUG*), *Cadherin-2* (*CDH2*, encoding N-cadherin), and *SRY-Box Transcription Factor 4* (*SOX4*) (Fig. 2F and fig. S1I). This is consistent with the important reduction in proliferation and clonogenicity described above (Fig. 1, D to F, and fig. S1A). GSEA analysis of the four AR mutants versus WT signatures evidenced again that V758A was not enriched in any of the PCa signatures in the Molecular Signature Database (MSigDB), as opposed to the significant enrichment demonstrated for F755V, Y764C, and Q799E (Fig. 2G). Accordingly, only these three mutant signatures were found positively enriched in a previously defined up-regulated gene signature strongly associated with poorer outcome in patients with PCa (Fig. 2H) (58).

Last, querying the collection of manually drawn Kyoto Encyclopedia of Genes and Genomes (KEGG) database evidenced an unexpected enrichment for the Y764C mutant in biological pathways associated with pathogen infection and immune response including coronavirus disease 2019 (fig. S1D), which was supported by the significant regulon enrichment in the mediator of type I interferon signaling, *STAT2* (fig. S1E), and the activation of the *Janus kinase/ signal transducers and activators of transcription (JAK/STAT)* pathway (fig. S1F) using the DoRothEA and the Pathway RespOnsive GENes (PROGENy) algorithms, respectively. Together, these data suggest that the observed differences in cellular phenotype between the different AR mutants are at least in part the result of a differentially reprogramed transcriptome in which WT and V758A show a less oncogenic and undifferentiated molecular phenotype compared to F755V, Y764C, and Q799E mutants.

AR-LBD interface residue mutations do not compromise domain folding but lead to reduced thermal stability and increased sensitivity to proteolysis

To study the possible structural impact of point mutants located at the AR-LBD dimerization interface, we produced and purified to homogeneity WT AR-LBD and its point mutants F755L, F755V, V758A, Y764C, and Q799E. Next, we characterized these recombinant proteins both biophysically using differential scanning fluorimetry (DSF) and biochemically through limited proteolysis assays (figs. S3 and S4). The results of these experiments demonstrated that all mutants are properly folded but have substantially lower thermal stability compared to the WT protein, as indicated by the reduced melting temperatures (T_m) (fig. S3, A and B). In line with the RNA sequencing (RNA-seq) results presented above, core dimer interface mutants F755V, F755L, and Y764C exhibited a remarkable drop in T_m compared to the WT protein (between 5° and 6°C), the latter being the most thermolabile of all the studied variants. By contrast, the T_m of mutants V758A and Q799E was

only 1°C lower than the WT AR-LBD protein, demonstrating WT-like stability (fig. S3, A and B). Energy estimations using FoldX based on previously reported structures of monomeric and dimeric AR-LBD also suggested that the studied missense mutations have an important impact on the domain stability (fig. S3C), both in its monomeric and putative dimeric conformations. Mutations of the core interface, F755V/L and Y764C, are predicted to be particularly deleterious for homodimeric AR-LBD (fig. S3C).

AR-LBD is a highly basic protein domain (isoelectric point: 8.94) with 14 arginines (fig. S4A) and 14 lysines outbalancing 11 negatively charged aspartate or glutamate residues. To assess whether the decrease in thermal stability of AR-LBD point mutants also manifests as an increased sensitivity to proteolysis, we incubated highly purified samples of WT AR-LBD and its point mutants with the endoproteinase, Arg-C, which cleaves peptide bonds at the C-terminus of Arg residues (fig. S4, B to E).

Again, the resulting cleavage pattern of V758A is most similar to that of WT AR-LBD (fig. S4, B, C, E, and F). Although the thermal stabilities of the two mutants are similar (fig. S3, A and B), the proteolytic patterns of V758A and Q799E differ notably (fig. S4, C to F and H). Mutants F755L (fig. S4, B, E, and G), F755V (fig. S4, C, E, and I), and Y764C (fig. S4, D, E, and H) have enhanced proteolytic susceptibility. In summary, point mutations of residues at the AR-LBD homodimerization interface appear to have an unanticipated global impact on the overall domain stability, as evidenced by notably lower T_m and enhanced sensitivity to proteolytic attack (figs. S3 and S4).

AR-LBD dimer interface mutants exhibit enhanced flexibility and distinct structural rearrangements both locally and at distant AF-2 and BF-3 sites

The results of the experiments described above demonstrate a large impact of AR-LBD dimer interface mutants on AR transcriptional function, stability, and sensitivity to proteolytic attack. To assess whether these differences are reflected by noticeable structural rearrangements, we expressed crystallized and refined at high resolution the x-ray crystal structures of the V758A, Y764C, F755V, F755L, and Q799E AR-LBD variants (Figs. 3 and 4). All mutant proteins crystallized as monomers in the orthorhombic space group ($P2_12_12_1$) (Figs. 3A and 4A and fig. S3D; see fig. S3E and Fig. 4B for comparison; Table 1). The "helical sandwich" fold typical of the nuclear receptor superfamily is conserved (3), and the hormone (DHT) is bound inside the LBP essentially as in WT AR-LBD (Figs. 3A and 4A). The root mean square deviations (RMSDs) for the equivalent Cα atoms between the WT structure [Protein Data Bank (PDB) 1T7T] and the V758A, Y764C, F755V, Q799E, and F755L mutants are 0.29, 0.33, 0.47, 0.52, and 0.54 Å, respectively.

Despite this overall conservation of the global protein fold, superimposition of the current mutant structures on previously solved structures of WT AR-LBD reveals important local structural changes on four specific distant sites of the domain (see Fig. 3A for an overall representation of the domain with these sites highlighted and Fig. 3, B to E for close-ups of these areas): the H5-S1-H7 area (from now on termed "R761 zone," described in detail below) (Fig. 3B), the L1-3 loop, H6, and the C-t end of H11 (Fig. 3C), two major functional sites, the BF-3 pocket comprising H9 and L9-10 (Fig. 3D), and the AF-2 pocket featuring the L3-4 loop and H12 (chaperone and coactivator binding sites, respectively) (Fig. 3E). In particular, several side chains of charged AF-2 residues
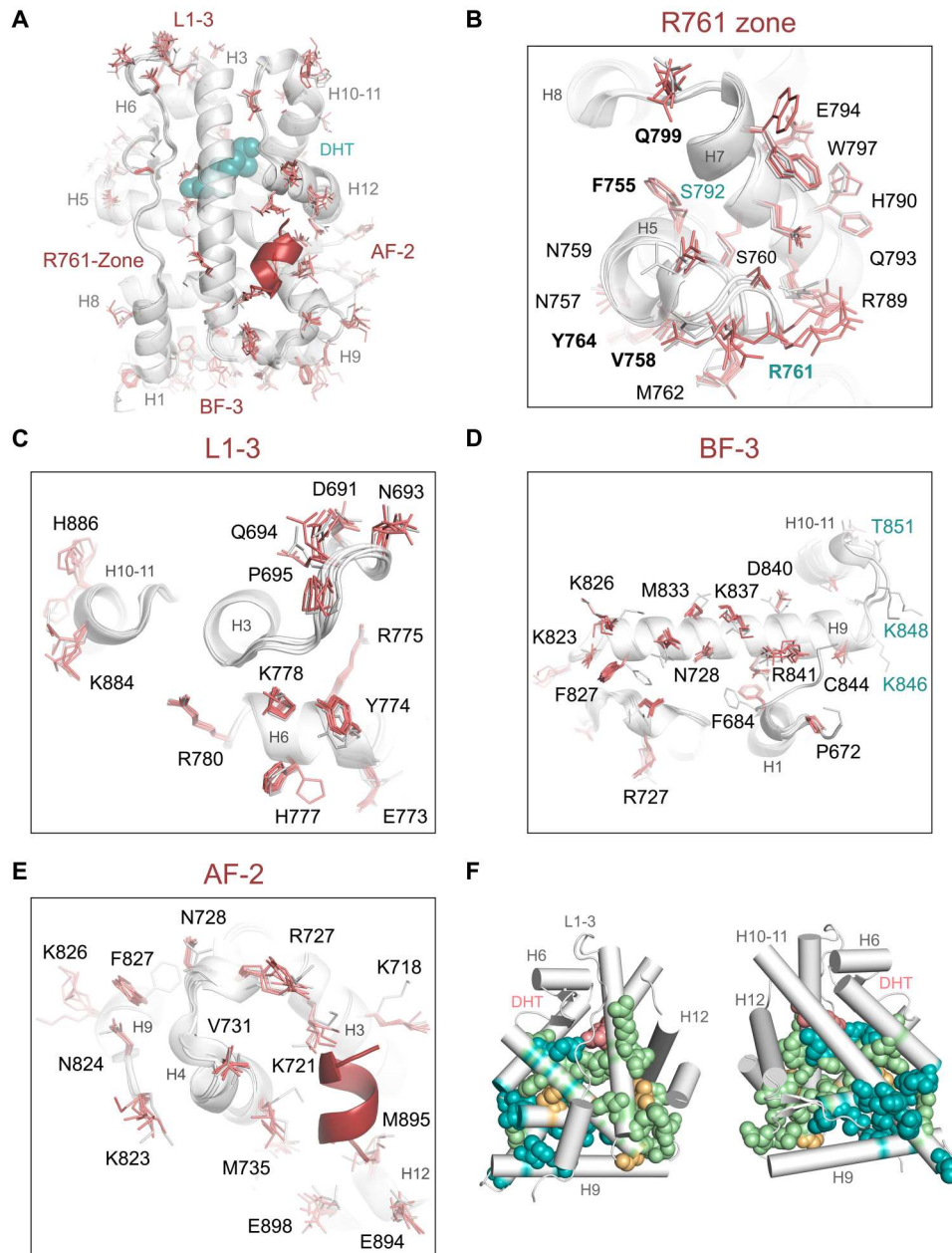
Fig. 3. High-resolution crystal structures of AR-LBD dimer interface mutants reveal local and long-range conformational changes. (**A**) Superimposition of current crystal structures of mutant AR-LBD on WT monomeric (1T7T) and dimeric (5JJM) forms of the domain. Secondary structure elements identical in all structures are depicted as a gray cartoon, with DHT as teal spheres and the AF-2-bound peptide (from 5JJM) in red. Large main- and/or side chain conformational changes cluster in four areas (B to E), highlighted by the major secondary structure elements (coral sticks). (**B**) Dimer interface core lined by H5 and H7, which, in addition to the studied point mutations [Phe[755] and Val[758] (H5), Tyr[764] (S1), and Gln[799] (H7)] features mostly residues with nonpolar/aromatic side chains, along with the positively charged Arg[761]. (**C**) The more distal part of the dimer interface formed by H3 and L1-3 [Tyr[774] and His[777] from (B) are shown for orientation]. In this area, several polar residues exhibit noticeable conformational changes. (**D**) BF-3 pocket, where multiple residues exhibit conformational changes, most notably those from H9. (**E**) AF-2 pocket, where in addition to the charge-clamp residues, Lys[721] and Glu[894], known to stabilize bound coregulators at this interaction site, the side chains of both charged (Lys[718], Arg[727], Lys[823], and Glu[898]) and aliphatic residues (Met[735] and Met[895]) display conformational variability. (**F**) Sector 1 (teal) comprises 17 residues in and around H5, H7, H8, H9, and H10-11 (Met[743], Phe[748], Gly[751], Arg[753], Leu[798], Ile[800], Thr[801], Met[808], Leu[811], Phe[814], Glu[838], Ile[842], Thr[851], Tyr[858], Thre[861], Lys[862], and Leu[864]), whereas sector 2 (green) features 20 residues mostly from H3, H5, H7, H8, S3, and H10-11 (Arg[711], Leu[713], Trp[719], Ala[720], Lys[721], Phe[726], Leu[729], Gln[734], Tyr[739], Trp[742], Gly[744], Met[746], Ala[749], Trp[752], Ser[754], Leu[791], Lys[809], Leu[813], Asp[820], and Arg[856]). Last, three residues (Gly[725] and Ile[738] at the AF-2 groove and Phe[805] at H7) belong to both sectors (yellow).
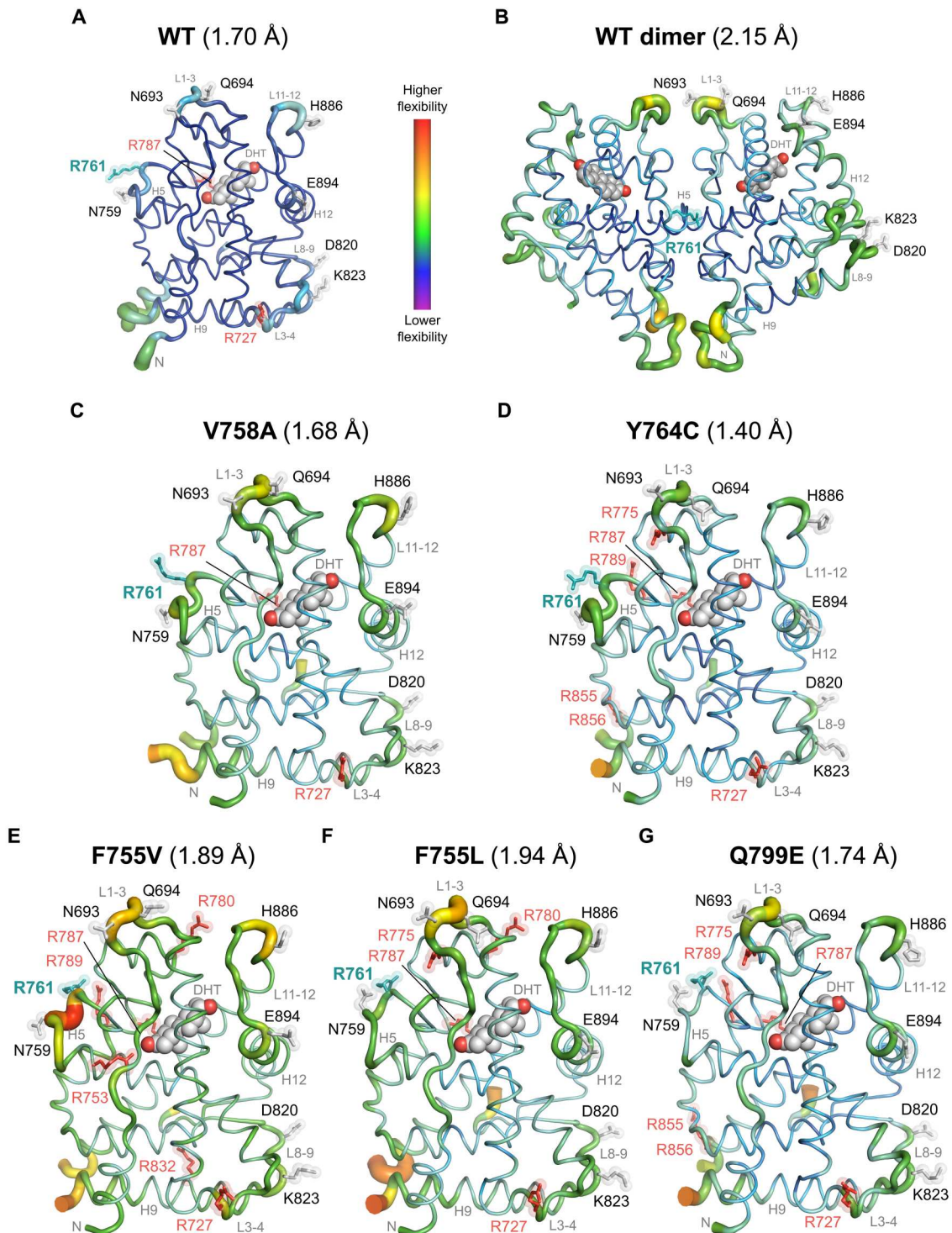
Fig. 4. AR-LBD dimer interface mutants display local flexibility differences. (**A** to **G**) Visualization of protein mobility for WT and AR-LBD mutant proteins. Proteins are represented as ribbons sized by temperature factors (B-factors) and colored according to the average B-factors of each residue (i.e., areas with larger atomic displacements appear thicker and are depicted with warmer colors (red, orange, and yellow), whereas those with lower thermal motion are shown thinner and with cold colors (green, blue, and violet). DHT molecules bound inside the LBP pockets are shown as gray spheres with oxygen atoms in red. WT AR-LBD·DHT monomer (A, PDB 1T7T) and dimer (B, PDB 5JJM) are shown for comparison. Note that all mutants exhibit a larger mobility than WT AR-LBD.

Table 1. X-ray crystallography data collection, refinement statistics, and model quality.

	V758A		Y764C		F755V		F755L		Q799E	
PDB code	**7ZU1**		**7ZTZ**		**7ZTX**		**7ZTV**		**7ZU2**	
Wavelength (Å)	0.979		0.979		0.979		0.979		0.979	
Resolution range	1.68	66.17– (1.71–1.68)	1.40	65.84– (1.42–1.40)	1.89	65.82– (1.93–1.89)	1.94	56.2– (1.99–1.94)	1.74	44.55– (1.77–1.74)
Space group	P2₁2₁2₁		P2₁2₁2₁		P2₁2₁2₁		P2₁2₁2₁		P2₁2₁2₁	
Cell constants a, b, c (Å) / α, β, γ (°)	55.62, 66.17, 70.95 / 90, 90, 90		56.39, 65.84, 72.82 / 90, 90, 90		54.57, 65.82, 70.37 / 90, 90, 90		56.18, 65.80, 72.31 / 90, 90, 90		56.51, 66.04, 72.42 / 90, 90, 90	
Molecules in the ASU	1		1		1		1		1	
Total reflections	176567 (4168)		247697 (9727)		143549 (9454)		84880 (3942)		147708 (8184)	
Unique reflections	29533 (1229)		53810 (2576)		20910 (1309)		18026 (1027)		28510 (1559)	
Multiplicity	6.0 (3.4)		4.6 (3.8)		6.9 (7.2)		4.7 (3.8)		5.2 (5.2)	
Completeness (%)	96.6 (80.4)		99.6 (98.2)		99.9 (100.0)		88.1 (79.8)		100.0 (100.0)	
Mean I/sigma(I)	10.3 (0.7)		18.8 (0.5)		8.8 (0.7)		10.4 (2.8)		12.3 (1.5)	
Wilson B-factor	27.1		27.0		38.2		22.8		26.1	
R-meas	0.084 (2.026)		0.030 (1.692)		0.116 (3.399)		0.093 (0.720)		0.089 (2.398)	
R-pim	0.033 (1.015)		0.014 (0.841)		0.045 (1.257)		0.042 (0.363)		0.039 (1.042)	
CC1/2	0.998 (0.364)		1.000 (0.395)		0.998 (0.364)		0.989 (0.854)		0.999 (0.337)	
Reflections used in refinement	28174		51127		19842		17086		27029	
Reflections used for R-free	1235 (4.2)		2619 (4.9)		1020 (4.9)		888 (4.9)		1433 (5.0)	
R-work	0.21		0.19		0.20		0.22		0.18	
R-free	0.25		0.22		0.25		0.26		0.22	
Total number of atoms / Protein / DHT ligand / Water	2135 / 2008 / 21 / 81		2161 / 2010 / 21 / 120		2041 / 1973 / 21 / 32		2066 / 1997 / 21 / 44		2080 / 1985 / 21 / 64	
RMS (bonds)	0.007		0.011		0.008		0.007		0.009	
RMS (angles)	1.420		1.828		1.606		1.500		1.581	
Ramachandran favored (%)	98.76		98.74		98.32		98.33		99.16	
Ramachandran allowed (%)	1.24		1.26		1.26		1.25		0.84	
Clashscore	5.32		1.23		3.47		2.47		3.7	
Average B-factor / Protein (main, side chains) / DHT ligand / Water	40.4 / 40.0 (36.9, 42.8) / 29.1 / 44.4		35.6 / 35.1 (32.0, 38.1) / 25.4 / 42.8		48.2 / 48.1 (44.2, 51.9) / 34.3 / 47.3		37.5 / 37.6 (34.3, 40.8) / 25.3 / 36.3		37.3 / 37.2 (33.3, 40.9) / 26.0 / 41.9	

exhibit conformational differences, most notably the so-called charge-clamp residues, Lys[721] and Glu[894], which are known to stabilize bound coregulators at this protein-protein interaction site (Fig. 3E). Regarding the BF-3 pocket, and in addition to charged/polar residues such as Arg[841] and Thr[851], also the aromatic Phe[827] exhibits a large flexibility (Fig. 3D). Noteworthy, Phe[827] and Arg[841] undergo major conformational changes upon small-molecule binding to this surface-exposed pocket (63). Loop L1-3 also exhibits side-chain conformational differences in several residues (Tyr[774], His[777], and Lys[778]), which we had previously identified as part of a secondary dimer interface in AR-LBD crystals to generate a tetrameric arrangement of the receptor (Fig. 3C) (6).

These structural variations are also reflected by an overall enhanced flexibility of all mutants compared to WT AR-LBD [average temperature factor (B-factor) of 21.2 for the monomeric AR-LBD; PDB 1T7T], as demonstrated by the higher B-factors of both main and side chain atoms in all variable regions (Fig. 4).

Residues with particularly higher B-factors in the mutants are Asn[693] and Gln[694] (L1-3), Arg[727] (L4-5), Asn[759], and Arg[761], a residue strictly conserved in AR from fish to humans, but not found in other steroidal receptors (H5 and loop H5-S1; fig. S3, F and G), Asp[820] and Lys[823] (L9-10), His[886] (H6), and Glu[894] (H12) (Fig. 4). Overall, mutants V758A and Y764C are most similar to the WT protein in this regard, while Q799E, F755L, and F755V exhibit increased flexibility in H5, L1-3, and L9-10 (Fig. 4, A to G).

Our previous statistical coupling analysis (SCA) (64) revealed that two groups of correlated residues or "sectors" define the internal circuits linking major interaction sites in the LBD of the related glucocorticoid receptor (GR). To analyze whether the AR-LBD dimerization surface is allosterically coupled to other functional regions, we also performed SCA analysis, which identified 40 residues grouped in two sectors in the upper half of the domain (Fig. 3, F and G). Sector 1 residues cluster around the domain N-terminus (except the DHT ligand, Arg[752]), while sector 2 comprises LBP and

AF-2 residues. Further, three residues common to both sectors are strategically located to cross-connect the LBP, AF-2, and BF-3 and dimerization interface (Fig. 3, F and G). Together, our results suggest that both sectors link functionally relevant regions thus coupling, e.g., ligand binding to dimerization, coregulator binding, or chaperone docking/release.

To further explore the LBD dynamics and possible allosteric couplings between AR-LBD functional areas, we performed four 1-μs-long molecular dynamics (MD) simulations for both WT AR-LBD and all the mutants (Fig. 5). The analysis of the time evolution of the RMSD for all the Cα atoms using the experimental structure of WT AR-LBD as reference confirms that the overall fold of the domain is stable against these point mutations, and all structures show global structural stability. Moreover, global conformations do not vary remarkably for any of the mutants, and their final RMSDs oscillate at around 2 Å (Fig. 5A). To evaluate the flexibility of the mutants in more detail, we analyzed how a given residue fluctuates around a specific position with time. To this end, we quantified the fluctuations for all residues using the averaged root mean square fluctuation (RMSF) value, averaged for the four MD replicas (Fig. 5B). As expected, more flexible regions correspond to those with higher B-factors in the current structures (compare Figs. 4 and 5). To analyze how specific mutations affect the dynamics of the different regions, we calculate the RMSF differences between WT AR and the studied variants (Fig. 5B). The stretch Lys[884]-Val[888] (H10-H11) presents, for all the mutants, a markedly decreased flexibility compared to WT (Figs. 5B and 3C). On the other hand, the L1-3 loop (residues Cys[687]-Asn[693]) is notably more flexible in the V758A and F755L mutants. This behavior is also observed in the Q799E mutant, although less pronounced, but neither in Y764C nor in F755V mutants. These two regions are located far from the mutated residues, suggesting that mutations in the AR-LBD dimerization site induce conformational changes in the AF-2 pocket and thus that dimerization and coregulator binding are allosterically coupled.

Next, and to complement the dynamic description of the impact of the different mutations, we quantified local conformational changes by calculating the differences in the average Cα-Cα distances between spatially neighboring residue pairs [extended up to the second coordination shell (SCS); ~9.1 Å]. The results of these $\Delta \overline{R}_{ij}$ analyses are presented in Fig. 5C. Overall, all mutant structures tend to have larger inter-residue distances compared to the WT protein, and some specific groups of residues show remarkable changes in their average pair distances. This is particularly true for residues Lys[884]-His[886] and Val[888]-Phe[892] at the C-terminal end of H10-H11 and the L11-12 loop (box A in Fig. 5C). In line with the experimental findings, the R761 zone shows important changes in all the mutants (residues Asn[759] to Tyr[764], L5-S1 loop). This region presents two different groups of moving residues, consisting of the stretch from Arg[789] to Phe[795] (H7) and Ser[754]-Val[758] of H4-H5 (boxes B1 and B2 in Fig. 5C, respectively). Furthermore, in all mutants, changes in average distances of residues Leu[729]-Asp[733] (L3-4 loop and N-terminal end of H4-H5) and Gly[821]-Asn[824] (S3-9 loop) are coupled (box C in Fig. 5C). However, in this case, changes are negative for mutations Q779E and F755V, both negative and positive for Y764C and V758A mutants, or positive for F755L. Last, residues Cys[687] to Gln[694] (L1-3) behave differently in each mutant. For F755L, this region shows negative changes in their average distances to residues Ala[688]-Arg[711] (L1-3 and H3) and the

Phe[765]-Leu[769] stretch (boxes D1 and D2 in Fig. 5C, respectively). Mutant V758A presents fewer changes in the average distances in the same regions, some of which are positive in the first one (box D1 in Fig. 5C). For the Y764C mutant, the first group of distances becomes completely positive, while the second one practically disappears. No noticeable changes were detected for mutants F755V and Q799E. In summary, residue pair distance analysis shows that the different interface mutations induce local conformational changes in AR-LBD. These changes are located far from the mutated residues in line with an allosteric mechanism. Moreover, although some changes are common to all the mutations, markedly different local responses were observed in specific AR regions.

The noncanonical AR-LBD dimerization mode is conserved upon single point mutations of dimer interface residues

Because the studied AR mutations are located at the noncanonical dimerization interface, we next wondered whether they might impair homodimer formation (Fig. 6). We had previously shown that AR-LBD dimerization in solution could be demonstrated with the homo-bifunctional cross-linker, bis(maleimido)ethane (BMOE), which cross-links residue Cys[687] from two monomers (6). To verify whether mutant proteins are able to dimerize as WT AR-LBD, we incubated purified samples of the recombinant proteins with either BMOE (spacer arm length: 8.0 Å) or a similar cross-linker with a slightly larger spacer arm, 1,4-bis(maleimido)-butane (BMB; 10.9 Å) and separated the reaction products by SDS–polyacrylamide gel electrophoresis (SDS-PAGE). The results of these experiments revealed similar patterns of AR-LBD homodimer formation in all cases, indicating that receptor homodimerization is not compromised by point mutations of interface residues (Fig. 6A).

Further, and to assess the possible impact of the studied mutants on the dimerization potential of AR-LBD mutants, we performed docking calculations using normalized interface propensity (NIP) (65) and optimal docking area (ODA) (66) (fig. S5). The computed binding energy of dimeric WT AR-LBD (PDB 5JJM; Fig. 4B; chains B and C, removing residues 845 to 851; Fig. 4B) was similar to that of V758A and Y764C mutants (assuming the same orientation as WT) and more favorable than that of the other mutants. Actually, the electrostatic energy contribution was much larger for WT than for any mutant, while the desolvation energy showed the opposite trend (fig. S5A). The size of the dimer interface as estimated from the buried surface area (BSA) was larger for WT than for the mutants, being V758A the one closest to WT (fig. S5A).

We also built alternative dimer arrangements by docking, based on WT (PDB 5JJM, chain B without residues 845 to 851) and current mutant monomeric structures (fig. S5B). The top ranked model in WT docking matched the x-ray dimer orientation (5.6 Å RMSD), with slightly better binding energy (fig. S5B). For all mutants, we also obtained similar orientations to the experimental dimer (RMSD < 10 Å), although not as the lowest-ranking models (fig. S5B). Binding energies for V758A and Y764C docking dimers were similar to those obtained by superimposition on the x-ray dimer, while in the rest of the mutants, the binding energy of the docking dimer was more favorable (although showing slightly higher RMSD). NIP-based interface hotspot residues predicted from docking (red residues in fig. S5C) were located at the x-ray dimer interface in WT and all mutants (except in F755V, which shows an additional NIP region around Asp[829], Arg[832], and

Fig. 5. Molecular dynamics study of the WT and mutant AR-LBD structures demonstrate overall domain stability coupled with local changes in flexibility. (**A**) Evolution of the RMSD for WT AR-LBD and the studied mutants along four independent MD runs. All structures converge demonstrating global structural stability. (**B**) Averaged RMSF of the four MD runs calculated for each structure: WT AR-LBD (black), V758A (blue), Y764C (purple), Q799E (green), F755L (violet), and F755V (red) (top plot). The remaining plots show the differences between the WT and mutant RMSF values. Residues with RMSF values higher than $+2\sigma$ or lower than -2σ (indicating decreased or increased flexibility compared to WT, respectively) are labeled. Only changes with values greater than twice their SDs were considered significant (red lines). Major changes in flexibility around the mutation site were detected only for the V758A mutant. Mutant F755V only shows a small change in this region, while Q799E does not present any changes near the mutated residue but around Asn[759] instead, in line with the experimental structure. Note that flexibility in the L5-S1 loop is remarkably higher in V758A, F755V, and Q799E compared to WT (blue). On the contrary, the C-terminal end of H10-11 shows lower relative flexibility in all the mutants. (**C**) Plots of the differences in average pairwise distances ($\Delta\overline{R}_{ij}$), with $\Delta\overline{R}_{ij} = \overline{R}_{ij,WT} - \overline{R}_{ij,mut}$, being $\overline{R}_{ij,WT}$ and $\overline{R}_{ij,mut}$ the average distances between Cα atoms of residues i and j along the MD trajectories of the WT and mutated structures, respectively. Red and blue represent positive and negative $\Delta\overline{R}_{ij}$ values, corresponding to residue pairs whose average distances decrease or increase due to the mutation, respectively. Only residue pairs with $\Delta\overline{R}_{ij} > 2.50$ or < -1.40, which represent the most significant distance changes, are shown.
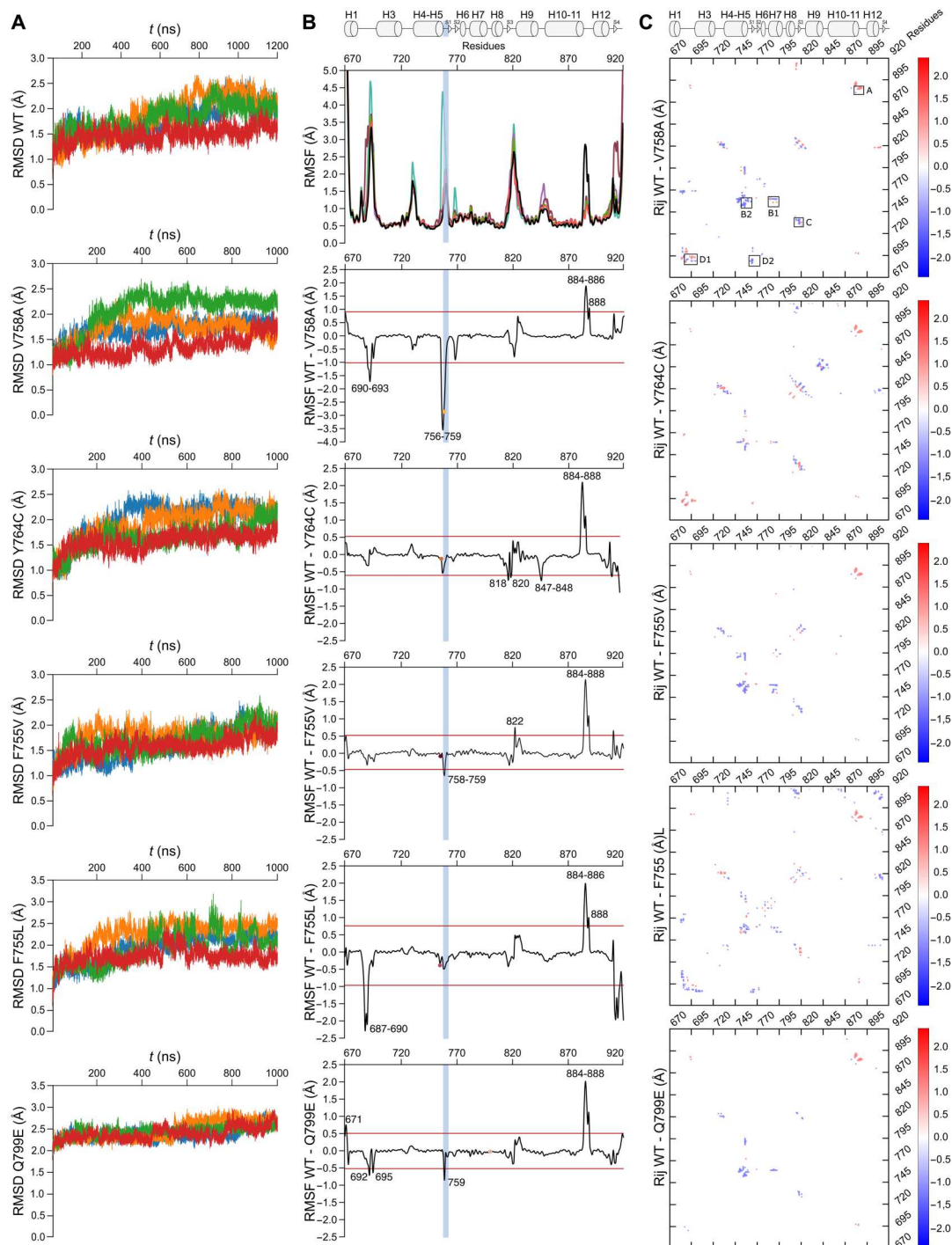
Ile[836]), with residue at position 755 appearing among the highest NIP values in all cases but in F755V. Desolvation areas predicted by ODA surface analysis were mostly located at the x-ray dimer interface in WT and all mutants (fig. S5D), indicating that a large part of the expected dimeric interface has favorable desolvation energy, especially the region around residue position 755. In general,

predicted dimer interfaces from docking experiments and ODA are consistent with the x-ray dimer orientation (6).
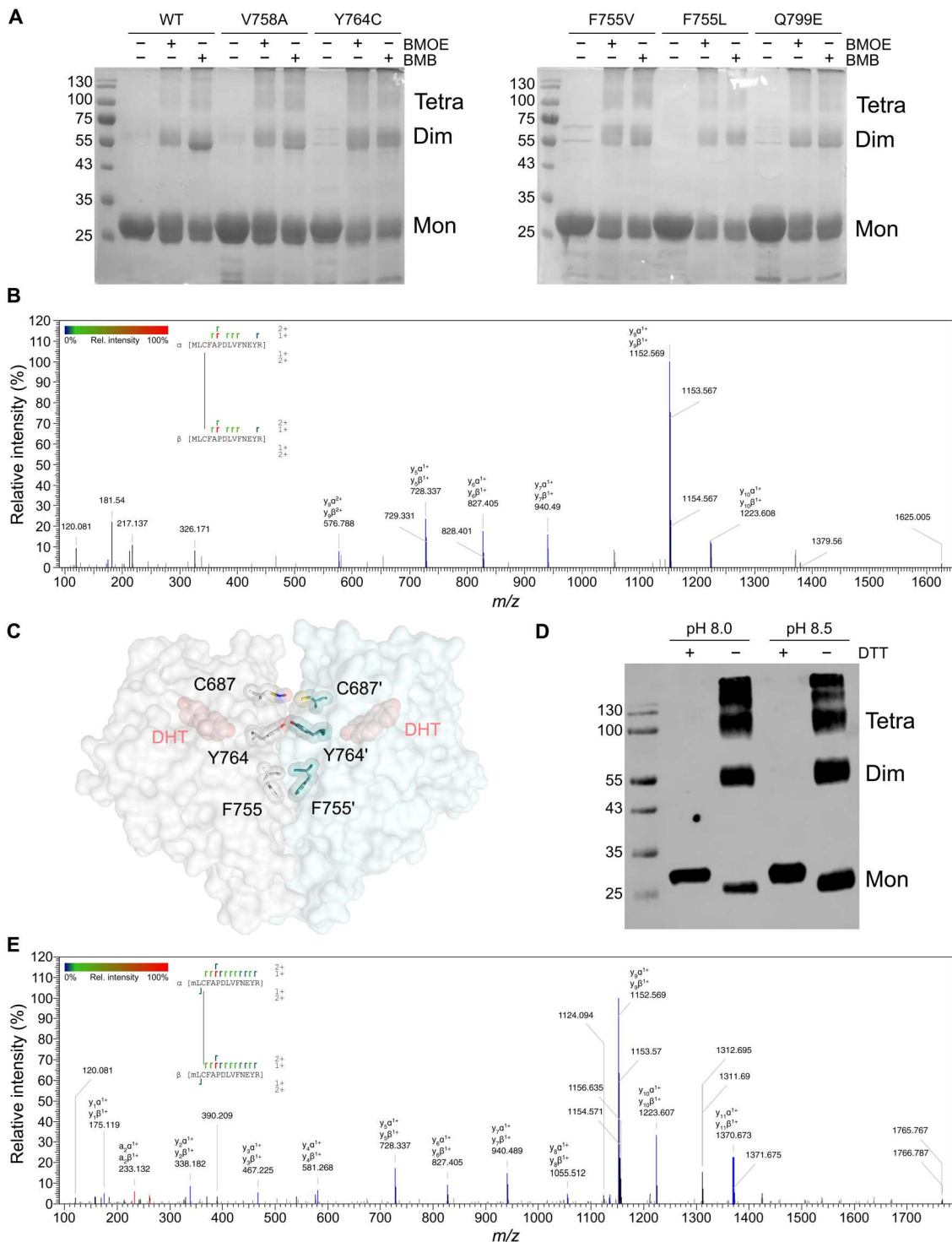
Fig. 6. Point mutations at the AR-LBD dimer interface do not impair homodimer formation, which is even enhanced in the Tyr[764]Cys mutant. (**A**) SDS-PAGE analysis of WT and mutant AR-LBD samples treated with the bifunctional cross-linkers, BMOE or BMB. Note similar intensities of bands corresponding to dimeric AR-LBD in all cases, indicating that homodimer formation is not compromised by any of the studied point mutants. (**B**) Representative MS/MS spectra identifying BMB-cross-linked tryptic peptides between Cys[764] residues from two LBD monomers. (**C**) Three-dimensional structure of the AR-LBD dimer (PDB 5JJM) in surface representation. Selected interface residues of both monomers [Cys[687], Tyr[764], and Phe[755] (as reference)] are shown as sticks. The DHT molecule is depicted as salmon spheres. (**D**) SDS-PAGE analysis of AR-LBD(Y764C) behavior under reducing (lanes 2 and 4, +DTT) and nonreducing conditions (lanes 3 and 5, −DTT). Note the spontaneous dimerization in solution when the protein is incubated under nonreducing conditions. (**E**) Representative MS/MS spectra demonstrating formation of a disulfide bridge between mutant Cys[764] residues from two LBD monomers. *m/z* stands for mass/charge ratio.

The recurrent point mutation Y764C highlights the ability of AR-LBD dimer interface to adopt different relative orientations in AR homodimers

AR variant Tyr[764]Cys was first identified in a PAIS family and has since been repeatedly reported in AIS and PCa individuals worldwide (36, 39, 42–48). Because this recurrent mutation introduces a solvent-exposed cysteine at the AR-LBD dimerization interface (Fig. 6C), we reasoned that the mutant protein would be more reactive, favoring formation of disulfide-bridged homodimers in solution. Y764C but neither WT AR-LBD nor other mutants tested rapidly forms covalent dimers in solution at basic pH as assessed by nonreducing SDS-PAGE (Fig. 6D). To directly prove that residues Cys[764]/Cys[764'] from each monomer are responsible for disulfide bridge–mediated dimerization in solution, bands corresponding to the AR-LBD(Y764C) dimer were excised from the gel and subjected to enzymatic digestion with endoproteinases trypsin and GluC. Tandem mass spectrometry (MS/MS) analysis of these digests allowed indeed the identification of peaks corresponding to Cys[764]–cross-linked peptides (Fig. 6E and table S3). The dimeric AR-LBD conformation previously identified by x-ray crystallography (Fig. 4B) (6) would not support reaction of neighboring Cys[764] residues (distance between Cβ atoms: 11 Å; Fig. 5C), but the recent structure of multidomain AR reveals the plasticity of this interface (7). Therefore, and to provide additional evidence of the plasticity of the AR-LBD homodimer, we analyzed by MS/MS the band corresponding to BMB–cross-linked, dimeric AR-LBD(Y764C) (Fig. 6B). The results corroborated the presence of a BMB-mediated linkage between Cys[764] Sγ atoms from two monomers (Fig. 6B and table S4).

The R761 zone undergoes large conformational rearrangements in AR-LBD point mutants

In the AR-LBD homodimer, the major interface is formed by polar and hydrophobic residues from H5, β strand S1, and their connecting loop, with additional contributions made by residues from H1 and H7-H9 and L1-3 (Fig. 7, A and B). The core dimer interface features residues Val[758]-Arg[761], along with the aromatic residues Trp[752], Phe[755], and Tyr[764], which are involved in an intricate network of hydrogen bond (H-bond) and van der Waals (VdW) interactions. Most notably, stacked residues Trp[752] and Phe[755] rigidify the H5-H5′ dimer interface, which is strengthened by strong VdW contacts of the latter with Pro[802] as well as by H-bonds between the guanidinium group of Arg[761] and the main chain carbonyl oxygen atoms of Glu6[79], Ala[680], and/or Glu[682] from the neighboring monomer (Fig. 7B). Unexpectedly, point mutations F755V/L (Fig. 7, F and G) and Q799E (Fig. 7H) resulted in a fully different conformation of H5-S1 loop residues compared to WT (Fig. 7C). Although residues Val[755]/Leu[755] occupy essentially the same position as the WT Phe[755], loss of stabilizing interactions mediated by the Phe[755] phenol ring ultimately result in the exposure of the downstream Asn[758]-Arg[761] sequence, which deviates by up to 4 Å from the more compact conformation commonly observed in structures of AR-LBD, and in which residue Ser[760] is essentially buried (Fig. 7, C to H). Most notably, the side chain of Arg[761] extends into bulk solvent and exhibits various degrees of freedom in the different mutants (Figs. 3B and 7, A to G). These residues are best defined by electron density in the F755L and Q799E crystals, in which the guanidinium group of Arg[761] is sandwiched between the carboxylates of its "own" Glu[773] and Asp[829] from a crystal neighbor (Fig. 7, G and

H). This extended conformation is stabilized by the side chain of Asn[759], which accepts an H-bond from the main chain N atom of Arg[761]. The proline-like conformation adopted by the preceding residue, Ser[760], is also noteworthy (Fig. 7G). Important contacts with a crystal neighbor constrain H5-S1 residues from larger displacements (Fig. 7, C to H). We reasoned that, in solution, these rearrangements could lead to even more extensive unfolding of the R761 switch zone. Important residue movements in this region were identified in our current MD simulations, some of which are larger than the deviations between mutant and WT in experimental structures (Fig. 5B and fig. S6).

Full-length AR is preferentially monomethylated in vivo by the methyltransferase, PRMT5, and methylation of Arg[761] is affected by AR-LBD dimer interface disease-linked mutations

Our structural analysis of AR-LBD point mutants that affect the dimer interface revealed important structural rearrangements, which parallel the differences in the transcription profiles of these variants (see above). These observations prompted us to explore possible functional consequences of the studied mutations. Residue Arg[761] adopts a markedly different, more exposed conformation in several mutants (Fig. 8, A to G), and it has been previously reported as a substrate of a major type II arginine methyltransferase with both mono- and symmetrical dimethylation activity, Protein arginine methyltransferase 5 (PRMT5), with important functional implications (18). To assess direct physical interactions between FL AR and endogenous PRMT5 in living cells, we performed proximity-ligation assays (PLA). The results of these experiments demonstrated strong AR-PRMT5 interactions in PC3-WT and PC3-Q799E cells, which were significantly reduced in PRMT5-silenced cells (Fig. 9, A and B; note the 50% loss of AR-PRMT5 interactions for both WT and Q799E). Furthermore, PLA experiments demonstrated arginine monomethylation of FL AR, as well as weaker symmetric dimethylation, which was reduced 50% upon incubation with the PRMT5-specific inhibitor, GSK595 (Fig. 9, D to F). In all PLA experiments, we observed heterogeneous patterns, with some nuclei showing strong AR-PRMT5 or methylation signals while others were practically devoid of these signals (Fig. 9, A and C). We also note that levels of Q799E mutant were remarkably lower in these experiments.

Western blot analysis of immunoprecipitated AR samples verified that Arg residues of both WT and mutant AR proteins were monomethylated in PC3 cells (Fig. 8H). Similar to the results of PLA experiments for the Q799E variant (Fig. 9C), the concentrations of mutant proteins were lower, and comparison of the relative intensities of bands corresponding to total and methylated AR fractions revealed that mutants were methylated to a lower extent. This feature is probably due to enhanced degradation of the mutant proteins, compared to WT AR (figs. S3, A and B, and S4) rather than reduced expression. In this regard, recombinant WT AR-LBD and its mutants are produced at similar levels in a heterologous system (Fig. 8I). In light of the structural information presented above, these findings strongly suggest that residue Arg[761] is preferentially monomethylated by PRMT5 in WT and AR-LBD mutants (Fig. 8H).

In the absence of structural information on the mechanism of recognition and processing of globular, macromolecular substrates by the methylosome (the hetero-octameric PRMT5·MEP50
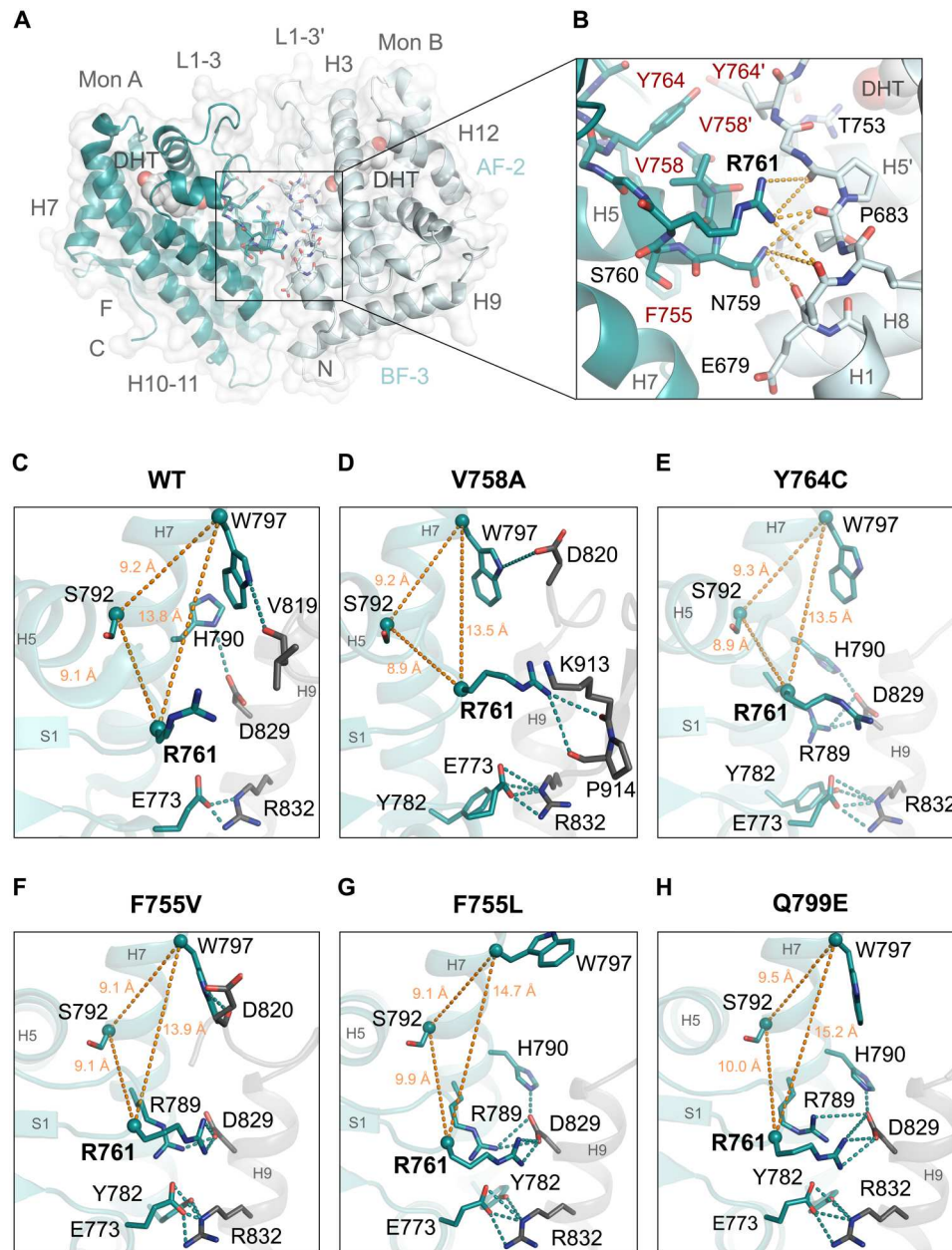
Fig. 7. The R761 zone undergoes large conformational rearrangements in AR-LBD point mutants. (**A**) Surface and cartoon representation of the AR-LBD·DHT dimer (PDB 5JJM). Residues comprising the core dimer interface are shown as color-coded sticks (oxygen, red; nitrogen, blue; carbon, teal or sky blue). (**B**) Close-up of the core dimer interface. Interface residues are shown as sticks and labeled. Major interdomain hydrogen bonds are represented as orange dotted lines. (**C** to **H**) Close-ups of the R761 zone in the crystal structures of mutant AR-LBD (teal-colored cartoons). The closest crystal neighbor is also shown in all cases (colored dark gray), to highlight major interactions due to the crystal packing. Residues involved in the crystal contacts are represented as color-coded sticks. Note the tighter contacts involving the Arg[761] side chain in mutants F755V (F), F755L (G), and Q799E (H) compared to WT (C), V758A (D), and Y764C (E), most notably salt bridges with the Asp[829] carboxylate from the neighboring monomer. Distances between the posttranslationally modifiable residues, Arg[761] and Ser[792], and from both of them to the reference residue, Trp[797], are also given.

complex) and to explore possible binding modes of AR, we performed docking experiments using the current structure of AR-LBD Q799E mutant and previously reported structures of the PRMT5·MEP50 complex (Fig. 9, G and H) (67–70). Similar interactions could be expected for WT AR and other point mutants. The results of these docking experiments suggest how the extended H5-

S1 loop in the AR-LBD would fit into the active site of the methyltransferase, supported by additional interactions of residues from the neighboring PRMT5 monomer (Fig. 9, G and H). Further, inspection of the docking solutions suggests that the AR-PRMT5 complex might be stabilized by additional interactions of AR-DBD with the N-terminal subunit of the transferase, while the
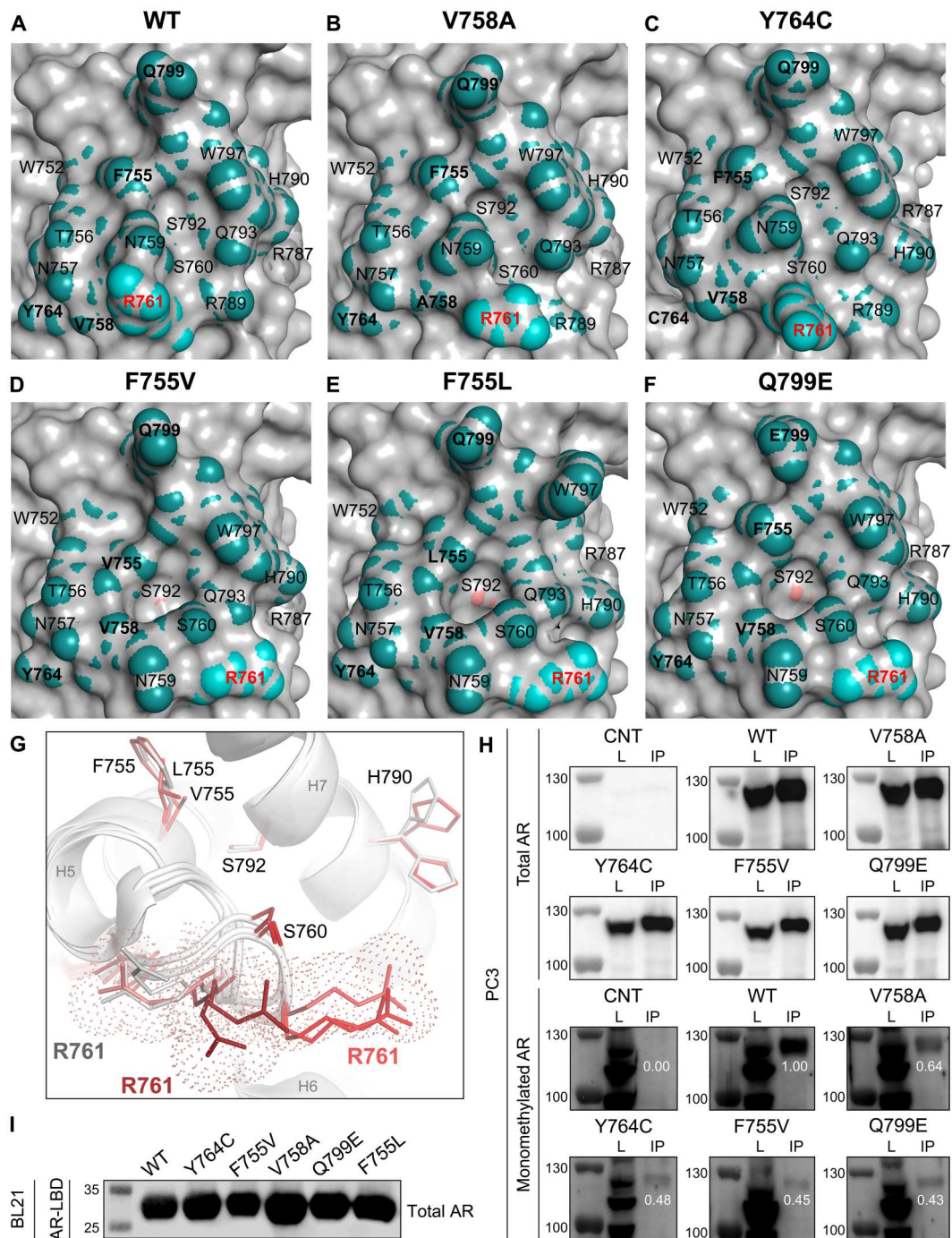
Fig. 8. Arg[761] is more solvent exposed in pathological AR mutations affecting on arginine methylation of the full-length receptor. (A to F) Surface representation of the AR-LBD pocket spanned by residues Trp[752] and Phe[755]-Val[758] (H5), Tyr[764] (S1), Arg[789]-Gln[793], Trp[797], and Gln[799] (H7) and Asn[759]-Arg[761] (loop H5-S1). All residues are shown as teal spheres superimposed by a gray surface to highlight the pocket topography. Note that conformational changes of Arg[761] (labeled in red) and surrounding residues remodel this pocket thus increasing solvent accessibility of Ser[792] (salmon), a key phosphorylation site by AKT kinase nested at its bottom. **(G)** Simplified cartoon representation of the Arg[761] zone depicting the major displacement of Arg[761] triggered by the dimerization mutants (different shades of red) relative to the WT position (gray). The pathological mutations induce a dislodgement of loop H5-S1, best appreciated by the different conformations adopted by the Arg[761] side chain: from an intermediate state in V758A and Y764C (dark red, facing the viewer) to a right-oriented, more solvent-exposed position in F755V, F755L and Q799E (in salmon). **(H)** Western blot analysis of total and monomethylated FL AR fractions in PC3 cell lines expressing transduced WT or point mutants of the receptor. L, total lysate; IP, immunoprecipitated fraction. A monoclonal antibody that specifically recognizes monomethylated arginine residues was used for WB. Monomethylated AR bands were double normalized against the total IP AR and against the monomethylated WT AR band (= 1.00), so that monomethylation levels of AR mutants are not biased by the amount of immunoprecipitated proteins. **(I)** Relative expression levels of WT and mutant AR-LBD recombinant domains in BL21 *Escherichia coli* cells.

Fig. 9. AR is preferentially monome-thylated in living cells by the PRMT5·MEP50 complex. (A) Representative PLA images demonstrating AR·PRMT5 physical interactions (red dots). Nuclei were counterstained with 4',6-diamidino-2-phenylindole (DAPI; blue). PRMT5-silenced cells (si-PRMT5) were compared to nonsilenced cells (si-NS). **(B)** Quantified PRMT5-AR interactions are shown (mean ± SEM, $n = 3$). Differences between si-PRMT5 and si-NS cells were calculated using a t test. **(C)** Whole-cell extracts from (A) were analyzed and quantified for AR, PRMT5, and tubulin expression by immunoblot. **(D)** Representative images from AR methylation assessed using PLA with anti-AR and pan-methyl antibodies recognizing mono- (MMA) or symmetrically dimethylated arginine residues (SDMA). Red dots correspond to detected MMA and SDMA WT AR, and nuclei counterstained with DAPI (blue). A PRMT5-specific inhibitor was used to verify that the methylation signal was PRMT5-dependent. **(E)** The number of detected MMA/AR and SDMA/AR is shown (mean ± SEM, $n = 3$). Differences between catalytically active and inhibited PRMT5 cells were calculated using a t test. **(F)** Whole-cell extracts from (D) were analyzed and quantified for total AR, MMA-, and SDMA-protein patterns and tubulin expression by immunoblot. Note that, while SDMA can be mediated only by PRMT5 and PRMT9, MMA can be catalyzed by type I and II PRMTs. This explains the larger impact of the PRMT5-specific inhibitor on the SDMA fraction. **(G)** Model of AR-LBD(Q799E) approaching the active site of the PRMT5·MEP50 methylosome. For simplicity, only a heterotetrameric (PRMT5)$_2$·(MEP50)$_2$ complex is shown (PDB 4GQB). Note that folded substrates such as AR-LBD would interact with two neighboring catalytic subunits, in addition to NTD-MEP50 and DBD-PRMT5 contacts. **(H)** Diagram of putative interactions between AR domains and the methylosome. **(I)** Summary of PTMs affecting the AR-LBD.
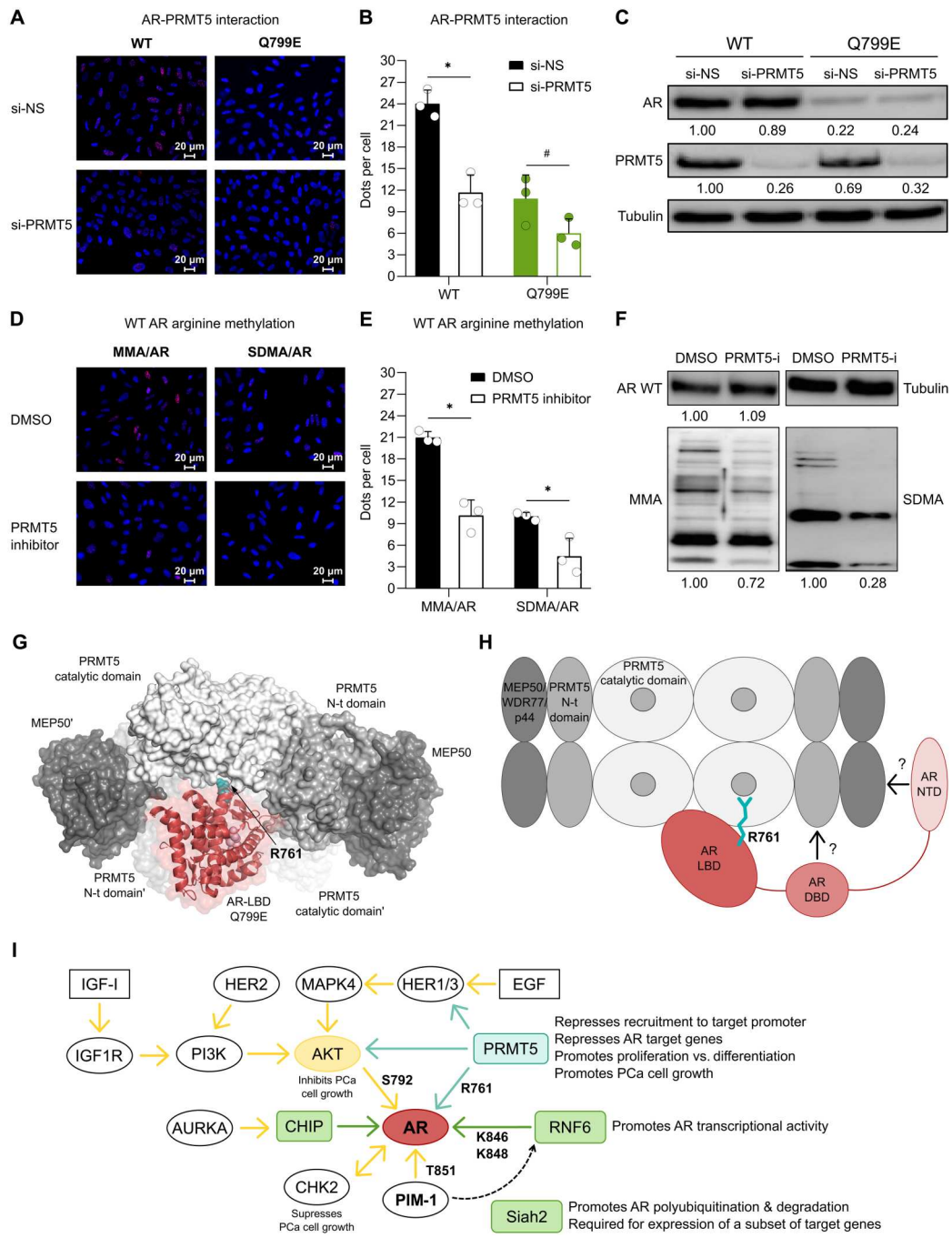
Note that PRMT5 regulates the cascade at different levels, including epidermal growth factor receptor (EGFR/HER1), protein kinase B (AKT), and AR. Phosphorylation (yellow), methylation (blue), and ubiquitination (green) pathways are shown: insulin-like growth factor 1 (IGF-I), insulin-like growth factor 1 receptor (IGF-1R), epidermal growth factor (EGF), epidermal growth factor receptor (HER1, 2 or 3), phosphoinositide 3-kinase (PI3K), mitogen-activated protein kinase 4 (MAPK4), aurora kinase A (AURKA), clonal hematopoiesis of indeterminate potential (CHIP), ring finger protein 6 (RNF6), checkpoint kinase 2 (CHK2), proto-oncogene serine/threonine-protein kinase (PIM-1) and E3 ubiquitin-protein ligase (Siah2).

MEP50/WDR77 component could recognize methylated Arg residues within the AR-NTD (Fig. 9, G and H). Synergy between these different interactions would ultimately provide the necessary energy to enforce structural rearrangements required to insert the nonglycine side chains of Ser[760] and Met[762] in the corresponding subsites of the enzyme, thus allowing methylation of residue Arg[761].

DISCUSSION

Although missense mutations of the *AR* gene have repeatedly been associated with conditions such as PCa and AIS (*29*), the molecular mechanisms of disease causation and the affected pathways remain poorly understood to date. Previous structural analyses of AR point mutants have been limited to internal residues that line the LBP, which are particularly relevant because of their association with resistance to anti-androgen therapy in patients with PCa (e.g., W742L, H875Y, and T878A) (*26–28*). Here, we present a thorough multidisciplinary analysis of the structural and functional impact of several mutations that are buried at the AR-LBD dimer interface (*6*) and which have been repeatedly linked to either AIS and/or PCa (F755L/V, V758A, Y764C, and Q799E). Although being essentially solvent-exposed residues in monomeric AR and thus unlikely to compromise the overall folding of the protein, we show that these disease-linked variants have significant structural and functional implications. Most notably, transcriptomic analysis demonstrated that, despite overall conservation of AR programs, notable differences exist at the transcriptional level between WT AR and most mutants, including key drivers of PCa progression such as *FOXA1* and *MYC*. In general, mutations at the AR-LBD dimer interface impaired AR's ability to halt proliferation and colony formation while retaining sensitivity to AR targeting drugs, consistent with a role for the nuclear factor as master regulator of differentiation (*58*). The growth-suppressive role for ligand-bound AR had previously been shown (*55*, *56*) and has been the basis for the proposed supraphysiologic testosterone treatment in patients with PCa that is being evaluated in clinical settings as part of the bipolar androgen therapy (*71*). Mechanistically, AR signaling has been shown to be dichotomous, promoting or repressing growth at low or high activity levels, respectively (*72*), and distinct transcriptional outputs have been identified for patients responding to supraphysiologic testosterone (*73*).

These large differences in transcriptional programs were paralleled by a largely reduced stability of the mutant AR-LBD modules, as indicated by notably lower T_m of up to 6°C and increased sensitivity to proteolysis in F755L/V and Y764C. Our current high-resolution crystal structures of the mutant domains reveal, in addition to changes in the targeted dimerization interface, an increased propensity to side chain movements of residues that cluster in previously described functional areas of the receptor: the exposed AF-2 and BF-3 pockets but also in the minor dimerization site identified in our previous crystal structure of multimeric AR-LBD and which evokes the tetrameric assemblies identified in living cells (*6*). Similar movements were also identified in MD simulations of mutant proteins (Fig. 5 and fig. S6). Structural rearrangements are particularly noteworthy in variants F755L/V and Q799E, in which residues of the R761 zone (H5-S1 loop) adopt a previously not observed, much more solvent-exposed conformation, which deviates by up to 4 Å from that observed in all previously reported structures of AR-LBD bound to both agonists and antagonists.

On the other hand, introduction of a cysteine in a solvent-exposed position at the dimer interface (Y764C) increases the propensity to nonproductive dimer formation, particularly in the crowded nuclear environment and likely further conformational changes in the FL protein. In this regard, the recently presented low-resolution cryo-EM structures of the core AR have revealed, in addition to an "entrenched" arrangement, which would correspond to our previously presented structure of dimeric AR-LBD (*6*), a more open or "splayed" assembly of AR monomers (*7*).

Our previous MD simulations of the V758A mutant indicated allosterically transmitted conformational changes in the AR-LBD (*41*). The current crystal structures of AR-LBD point mutations that affect the dimerization interface confirm and extend these observations. These replacements induce conformational changes at areas located in the diametrically opposed pole of the domain, most notably the AF-2 binding pocket (Figs. 1B and 3E). This is the first time that a mutation in the AR-LBD dimerization site has been linked to conformational changes in the AF-2 pocket, suggesting that dimerization and coregulators binding are allosterically coupled. Careful inspection of the crystal structures supported by MD and SCA analyses suggests allosteric pathways connecting the dimer interface with the LBP and the AF-2 and BF-3 sites in AR-LBD.

Previous investigations have revealed several functional defects in the studied mutants, including a lower affinity for agonists, which, at least in the case of Y764C, was shown to result from a more rapid dissociation of ligands without significant changes in the LBP, a significant to near complete loss of NTD-LBD (N/C) interactions, and a largely reduced transcriptional activity, particularly at physiological DHT concentrations (summarized in table S2). Together, these functional findings are in line with our current structural observations of increased mobility of AR-LBD mutants and have important consequences for the structure-function relationship of the receptor. First, the overall decrease in domain stability together with subtle displacements of AF-2 residues might impair both intra- (N-/C-terminal) and intermolecular interactions (with coactivators and corepressors). Conversely, the presence of the NTD would seem to stabilize the LBD upon N-/C- interactions, as suggested by the lower thermostability of a double mutant with a shortened polyQ stretch in the NTD in addition to the Y764C point mutation (*43*). This is also in line with the cryo-EM structures of FL AR, which revealed a compact conformation with a central LBD surrounded by the NTD (*4*, *7*), and with our recent identification of NTD-LBD interactions (*74–75*). Second, even mutations that do not affect the LBP directly can have a profound impact on DHT affinity, by facilitating its dissociation from the internal binding site. In this regard, hormone trafficking in and out the LBP is likely to involve displacements of residues in the H5-S1 loop similar to the ones observed in our current crystal structures or perhaps of a larger magnitude. N/C interactions of the Q799E mutant were normal, however (*48*), highlighting the unique molecular fingerprint of each mutation.

The PCa-associated transcription factor, estrogen-responsive gene (ERG), was previously shown to recruit protein arginine methyltransferase PRMT5 to AR-target genes (*18*). PRMT5 then methylates AR at position 761, ultimately down-regulating AR transcriptional activity. Here, we corroborate and extend these findings by showing a direct physical interaction of endogenous PRMT5 with both WT and the Q799E mutant of FL AR in living cells.

Further, we verified that AR is both mono- and, to a lesser extent, symmetrically dimethylated in cells in a PRMT5-dependent manner (Fig. 9, A to F). The presence of nonglycine residues both before and after Arg[761] would seem to make its methylation less favorable than canonical Gly-Arg-Gly motifs, in light of current structural evidence for PRMT5 (68–69) and other methylases (76). However, a recent systematic analysis of the human methylome has revealed a large number of substrates with bulky side chains preceding and/or following the modified arginine (77). Our docking experiments suggest that Arg[761] processing by the octameric (PRMT5)$_4$·(MEP50)$_4$ heterocomplex known as methylosome would depend on secondary interactions of residues in the immediate vicinity of the methylated arginine, on the one side, and exposed residues of the PRMT5 catalytic domain and the N-terminal subunit of a neighboring molecule in the methylosome, on the other. Substrate recognition might be assisted by additional interactions with the highly acidic noncatalytic subunit of the methylosome, MEP50/WDR77, which have been shown to orient substrate histones toward the buried active site of PRMT5 (78). A summary of predicted AR interactions with the methylosome that might ultimately determine specific recognition and processing of Arg[761] is schematically presented in Fig. 9 (G and H).

Although the more exposed, protruding conformation of Arg[761] in AR-LBD mutants would favor recognition and processing by the methylosome, we have actually observed a decrease in the total and methylated fractions of the studied AR mutants in cells. Point mutants of the AR-LBD are unlikely to affect protein expression, and we have observed similar expression levels of recombinant WT AR-LBD and its mutants. Therefore, this apparent contradiction points to an enhanced degradation of mutant AR protein. AR is polyubiquitinated by several E3 ligases (Fig. 9I), followed by its degradation in the proteasome. The tumor suppressor, C terminus of Hsp70-interacting protein (CHIP), appears to be particularly relevant in this regard, as it couples the chaperone machinery to AR degradation, inducing mitotic arrest (79, 80). Of particular clinical relevance, CHIP has been shown to modulate sensitivity to anti-androgen therapy in advanced PCa (81). These findings are also important with regard to the current development of proteolysis targeting chimeras as pharmacological alternatives for PCa treatment (82, 83).

Multiple additional connections between the PRMT5·MEP50 methylosome, AR pathophysiological activity, and PCa etiology have been reported. PRMT5 functions as an epigenetic activator of AR transcription in PCa (84), while the noncatalytic methylosome component, MEP50 (also termed androgen coactivator p44), has been previously identified as an AR interactor linked to PCa progression, which enhances AR-driven gene expression independently of PRMT5 catalytic activity. Accordingly, MEP50 expression levels are higher in PCa tissue than in adjacent, normal prostate tissue (85), and it has been associated with androgen-independent PCa (86). Further, MEP50 is required for homeostasis of prostate epithelial cells by controlling the proper expression of AR-target genes, and its translocation from the nucleus into the cytoplasm in PCa cells results in exacerbated proliferation of prostate epithelial cells (87). Together, the close relationship between methylosome and AR activity at the light of our current observations provokes a systematic analysis of AR methylation in patients with PCa and suggests avenues for therapeutic intervention, in particular in *TMPRSS2:ERG*-positive PCa (18).

Another important PRMT5 substrate, AKT kinase, is also methylated at a noncanonical sequence that resembles the AR-LBD modification site (Gln-Arg-Leu) (88). The side chain of the methylated arginine residue, Arg[391], is fully buried in the AKT protein core, indicating that large conformational changes are not uncommon in PRMT5 substrates. This finding is also relevant because AKT has been shown to phosphorylate AR at two canonical RXRXX(S/T) sites, Ser[213] in the NTD and Ser[792] in the LBD (12–15). Noteworthy, Ser[792] is located close to Arg[761], and it is more exposed in the mutants with an open H5-S1 loop. However, we have not detected significant differences in the degree of phosphorylation between WT and mutant AR.

Inspection of the AR-LBD 3D structure reveals that the dimerization interface comprises, in addition to Arg[761] and the nearby Ser[792], several residues that have been previously reported as targets of PTMs (Figs. 1A and 9I). This extended patch includes in particular the pair of lysine residues at positions 846 and 848, which are ubiquitinated by RNF6 to modulate coactivator recruitment and AR transcriptional activity (16). Last, residue Thr[851] is phosphorylated by the PIM-1L isoform of this Ser/Thr kinase, which stabilizes AR by recruiting RNF6 (17). The phosphomimetic Thr[851]Asp mutation resulted in increased transcriptional activity due to enhanced recruitment of coactivators at AF-2 (89), mirroring the impact of several point mutations at the dimer interface characterized in the current work. Together, this AR surface emerges as a major hotspot for PTMs (a summary of AR-LBD PTMs and their functional consequences is given in Fig. 9I). These findings underscore the realization that PTMs regulating DNA accessibility and transcription not only are not limited to histones but also affect also other elements of the transcription machinery (extended histone code) (90). Future investigations should depend on the cross-talk between PTMs and AR quaternary structure including interdomain motions and allosteric pathways connecting the different functional areas of the nuclear factor and their impact on its interactions with specific coregulatory proteins and its proteasome-mediated degradation.

In summary, the results of our multidisciplinary approach reveal a complex landscape of structure and function alterations induced by mostly conservative mutations that affect the dimerization interface of the AR-LBD, which opens various avenues for structure-guided modulation of AR function. The characterization of AR mutations presented here through a combination of complementary structural (x-ray crystallography coupled with docking experiments and MD simulations) and functional assays including transcriptome analysis could be straightforwardly extended to other pathological AR mutants including other oncogenic forms of the receptor. Early prognosis and precision pharmacology of AR-linked diseases would benefit from this integration of structural and cell biology studies under consideration of the interplay between AR mutations and PTM-driven pathology. Eventually, it might be possible to comprehensibly link all AR mutations to specific PCa subtypes, as has been achieved for the related estrogen receptor in breast cancer (21–22), as an important step toward truly personalized treatment of patients with PCa.

Our results open various avenues for structure-guided modulation of AR function. The future of precision pharmacology to tackle AR-linked diseases and also for the prognosis and treatment of patients with PCa needs to integrate structural biology with studies of cellular effects of mutations and PTM-driven pathology.

MATERIALS AND METHODS
Cell lines and plasmids

PC3, DU145, LNCaP, 22rv1, and RWPE-1 cell lines were purchased from and authenticated by ATCC (American Type Culture Collection). For maintenance, cells were cultured in RPMI 1640 or Dulbecco's modified Eagle's medium (DMEM), respectively, supplemented with 10% fetal bovine serum (FBS). For functional assay, cells were depleted of androgens using 10% charcoal-stripped serum (CSS; Thermo Fisher Scientific). Site-directed mutagenesis of a commercial lentiviral AR plasmid (pLENTI6.3/AR-GC-E2325, plasmid #85128, Addgene) was conducted to generate variants AR-F755V, AR-V758A, AR-Y764C, and AR-Q799E. For lentivirus production, human embryonic kidney 293FT (HEK293-FT) cells were cultured in DMEM (Thermo Fisher Scientific), and the lentiviral packaging vectors psPAX2 and pCMV-VSV-G were cotransfected in polyethylenimine (1 mg/ml) containing Opti-MEM (Thermo Fisher Scientific). After viral transduction using supernatants supplemented with polybrene (8 μg/ml), PC3 cells were incubated for 48 hours and selected with blasticidin (5 μg/ml) to generate control, WT AR, and mutants cell lines.

Luciferase reporter assay

To assess AR transcriptional activity, a luciferase-based assay was performed in PC3 cells, which were seeded (15,000 cells per well) in white with clear flat-bottom 96-well plates (RPMI 1640 media supplemented with 10% CSS). After 24 hours, 50% confluent cells were transfected using a Lipofectamine 2000 transfection reagent (Thermo Fisher Scientific), following the manufacturer's instructions. Renilla luciferase expression is controlled by a constitutive promoter for normalization (pRL-TK Renilla luciferase, Promega). On the other hand, Firefly luciferase plasmid (pARE-4X-Luciferase) contains four androgen response elements (AREs) cloned in tandem into pGL3 (Promega) (91). Transfection was performed using 100 ng of pARE-4X-Luciferase and 10 ng of pRL-TK Renilla luciferase. Both luciferases are monomeric and neither requires posttranslational processing, so they can function as genetic coreporters immediately upon translation.

Transfection mixes were prepared in Opti-MEM I (Thermo Fisher Scientific). Six hours after transfection, the medium was aspirated and replaced with RPMI 1640 media supplemented with 10% CSS. For the assay testing the transactivation level of AR mutants, cells were stimulated 24 hours after transfection for 4 hours with vehicle or 20 nM DHT. For luciferase assay testing AR mutants' resistance to PCa treatment drugs, cells were treated for 30 min with abiraterone (40 or 80 μM) or enzalutamide (50 or 200 μM) before 20-nM DHT stimulation for 4 hours. Luciferase activity was measured after cell incubation with the corresponding compounds with the Dual-Glo Luciferase Assay System (Promega) using an EnSpire Alpha plate reader (PerkinElmer). After background subtraction, the ratio of firefly to Renilla luciferase activity was calculated. Assays were performed in three independent experiments with five internal replicates each. GraphPad Prism 8.0 software was used to perform the statistical analyses using t test, once confirmed the normal distribution of the values.

Functional cell assays
Colony formation and proliferation assays

Approximately 30,000 PC3 cells were seeded in six-well plates and grown in RPMI 1640 media supplemented with 10% CSS, in two independent replicates for each experiment. The next day (day 1), cells were stimulated with 20 nM DHT. The stimulation was repeated every 2 days. Colonies were grown until day 9 and stained with crystal violet [0.5% (w/v) in 10% ethanol and 90% formaldehyde]. After 30 min of incubation and several washes with water, colonies were scanned and quantified using ImageJ software (https://imagej.nih.gov/ij/). Colony formation capacity was normalized to control cells. Statistical analysis was performed using t test, showing the differences with respect to PC3 WT AR. For colony formation assays in other cell lines, cells were seeded on the basis of their proliferation rate (DU145: 8000 cells per well; RWPE-1: 20,000 cells per well; 22Rv1: 30,000 cells per well; LNCaP: 80,000 cells per well). While DU145 and RWPE cells were cultured in CSS for this assay, 22Rv1 and LNCaP were cultured in FBS to prevent them from stopping proliferation. In all cases, media were supplemented with increasing concentrations of DHT.

Proliferation assays

Cells were trypsinized and counted (with trypan blue stain to discriminate living cells) every 2 days, starting at day 3 and finishing at day 7, to follow the time course growth. To compare proliferation at day 7, the number of cells of each PC3 variant was normalized to their corresponding nonstimulated control (without DHT). Statistical analysis was performed using t test, showing the differences with respect to PC3 WT AR.

MTT cell viability assays

Approximately 4000 cells ($n = 6$) were seeded in 96-well plates in RPMI 1640 media containing 10% CSS. Cells were supplemented the next day with DHT combined with abiraterone acetate (Memorial Sloan Kettering Cancer Center), enzalutamide (MDV3100; Sigma-Aldrich), or apalutamide (Janssen) at different concentrations. After 72 hours, cells were treated for 3 hours with 10 μl per well of MTT [3-(4,5-dimethylthiazol-2-yl)-2,5-diphenyltetrazolium bromide; 5 mg/ml], a yellow tetrazole that is reduced to purple formazan crystals by living cells. Formazan crystals were dissolved with 100 μl of solubilization buffer (10% SDS and 10 mM HCl) for 3 hours. Plates were read at optical density = 560 nm in a spectrophotometer, and then the percentage of viable cells compared to the untreated wells was determined. In the case of abiraterone, the inhibitory concentration was calculated using nonlinear regression fit in GraphPad Prism 8.0 software, normalizing to untreated cells. Statistical analysis was performed using parametric paired t test comparing each PC3 AR-mutant regression curve versus PC3 WT AR. Because of drug resistance of PC3 cells against enzalutamide and apalutamide, data did not fit nonlinear regression models. To compare enzalutamide and apalutamide resistance, normalized cell viability (at 50 μM enzalutamide or 100 μM apalutamide) was expressed as a fold change percentage with respect to WT AR. Statistical analysis was performed using a t test, showing the differences between the PC3 WT AR and its mutants. For viability assays of other cell lines, cells were seeded to reach confluence (90%) at the end of the experiment (DU145: 2500 cells per well; LNCaP, 22Rv1, and RWPE-1: 5000 cells per well). While DU145 and RWPE were cultured in CSS for this assay, 22Rv1 and LNCaP were cultured in FBS to prevent them from stopping proliferation. In both cases, media were supplemented with increasing concentrations of DHT.

Immunoprecipitation and Western blotting

For immunoprecipitation (IP) of FL AR, PC3 cells were scraped off the plate and transferred to a microcentrifuge tube using lysis buffer (LyB) containing 50 mM tris, 150 mM NaCl, 0.2% NP-40, and 10% glycerol supplemented with protease inhibitor cocktail (Roche), 1% phosphatase inhibitor cocktail 3 (Sigma-Aldrich), and 0.5% phenyl-methylsulfonyl fluoride (Sigma-Aldrich) (in following, inhibitor mix). Samples were sonicated on ice three times for 5 s each, 30% amplitude, and centrifuged. IP of the collected supernatant was performed using magnetic beads (Protein G and Protein A Mag Sepharose beads, Thermo Fisher Scientific). AR XP (1:50; Cell Signaling, 5153) and immunoglobulin G (IgG; 1:50; rabbit IgG polyclonal–isotype control, Abcam) antibodies were preincubated for 1 hour with 25 µl of A + G beads (1:1) at 4°C, and cell lysates (1.6 mg) were precleared with 5 µl of A + G beads (1:1). Beads were removed from the precleared lysates and then transferred into AR or IgG tubes for IP at 4°C overnight in a rotating wheel. Afterward, beads from the negative control (IgG tubes) and the immunoprecipitated samples were washed twice with LyB and five times with LyB lacking NaCl. Last, beads were eluted with 70 µl of Laemmli buffer containing 10% β-mercaptoethanol for 5 min at 98°C, and samples were analyzed by Western blotting.

For Western blot analysis of total protein extracts, PC3 cells were lysed with 1× radioimmunoprecipitation assay (RIPA) buffer [10 mM tris-HCl (pH 7.5), 0.1% SDS, 1% deoxycholate sodium salt, 1% triton X-100, 0.15 M NaCl, and 1 mM EDTA] supplemented with inhibitor mix. Proteins (30 µg per lane) were resolved by SDS-PAGE and transferred onto a polyvinylidene difluoride membrane (GE Healthcare, Amersham), which was blocked with PBS-T (phosphate-buffered saline and 0.1× Tween 20) containing 5% bovine serum albumin (Sigma-Aldrich). Primary antibodies for Western blot were incubated at 4°C overnight: anti-AR (1:500; Abcam), anti-mono methyl arginine (R*GG) (1:500; Cell Signaling), and anti-rabbit IgG horseradish peroxidase–linked antibodies (1:10,000; Cell Signaling). HRP-conjugated secondary antibody was incubated for 1 hour at room temperature. The ECL Plus Western Blotting Detection Kit (Thermo Fisher Scientific) was used for detection in a ChemiDoc MP Imaging System (Bio-Rad).

Transcriptomic analysis

For transcriptomic analysis, approximately 500,000 PC3 cells were seeded in 10-cm plates in RPMI 1640 media supplemented with 10% CSS (hormone depletion conditions) ($n = 3$). After 48 hours, cells were stimulated with 20 nM DHT for 4 hours and collected. RNA was purified using the Maxwell RSC simplyRNA Tissue Kit (Promega), following the manufacturer's instructions. RNA quality control, library preparation, 2 × 100 bp, >25 M paired-end reads, and stranded mRNA sequencing (RNA-seq) were performed using an Illumina HiSeq2500 platform. RNA-seq lanes were joined and reads were mapped with STAR (92) to the primary assembly of the human reference genome (GRCh38) in conjunction with the complete gene annotation file available in GENCODE (93). The gene read count was performed with the STAR parameter - quant-Mode GeneCounts. Results indicate, on average, 90% of reads uniquely mapped in all samples; around 80% of the reads are overlapping genes.

We used the IDEAmex service (94) to perform differential expression analysis using DESeq2 (95) and limma methods (96). The count matrix was filtered considering 5 counts per million (CPM). To define DEGs, we considered an absolute $\log_2$ fold change ≥ 1 and an adjusted P value or false discovery rate (FDR) ≤ 0.05. The following DE analyses were performed: PC3 control versus WT AR and point mutants F755V, V758A, Y764C, and Q799E, as well as WT AR versus PC3, F755V, V758A, Y764C, and Q799E. To identify the intersection of genes differentially expressed between contrasts, we used the function UpSet from the package Complex heatmaps (97). Volcano plots were generated using the Enhanced Volcano R package on DESeq2. AR targets were recovered from DoRothEA (57).

For PCA, raw counts were filtered to have at least three samples with a CPM ≥ 5. Counts were transformed using the VST function (98). The PCA was calculated with the plotPCA function in DESeq2 and visualized with the ggplot2 package. For the VST data, we calculated the Euclidean distances between samples using the R function dist. We plotted the sample distance matrix with the rows/columns arranged by the distances, manually providing sampleDists to the clustering distance argument of the pheatmap function.

Enrichment analysis

GSEA (99) was performed to assess the enrichment of the different mutant AR signatures against a reference signature of DEGs between control versus WT AR ranked according to the $\log_2$ fold change value and the clusterProfiler R package (100) on DESeq2 results. GSEA was also used to ascertain the enrichment in selected gene sets that match against the search for "prostate cancer" in MSigDB or the entire Biological Pathways collection in the KEGG database. We performed GSEA against PCa malignant signatures FOXM1, CENPF, and FOXM1 + CENPF for each DESeq2 result between PC3 control versus WT AR, F755V, V758A, Y764C, or Q799E. Signatures recovered are defined as top 200 up- and down-regulated DEGs (58).

Transcription factor activity was estimated with the DoRothEA R package (57) using results from the limma package (96) between PC3 versus WT AR or F755V, V758A, Y764C, or Q799E mutants. We estimated activity for pathways involved in cancer with PROGENy (101). DEG results between PC3 control versus WT AR, F755V, V758A, Y764C, or Q799E using as input the list of genes ranked by the $\log_2$ fold change.

AR target genes expression analysis by RT-qPCR

For qPCR, approximately 300,000 PC3 cells were seeded in six-well plates in duplicates in RPMI 1640 media supplemented with 10% FBS. After 48 hours, 70% confluent cells were hormone-depleted by using RPMI 1640 media supplemented with 10% CSS. After 24 hours, cells were stimulated with 20 nM DHT for 4 hours and collected. RNA was extracted using a TRIzol reagent according to the manufacturer's instructions. After DNA digestion (deoxyribonuclease, Amplification Grade, Invitrogen), cDNA was obtained using the High-Capacity cDNA Reverse Transcription Kit (Applied Biosystems). Total cDNA was diluted 1:10, qPCR was performed using PowerUp SYBR Green Master Mix (Applied Biosystems), and plates were read with a LightCycler 480 (Roche). The following reverse transcription (RT)–qPCR primers were used to amplify glyceraldehyde phosphate dehydrogenase (GAPDH; 5′-CATCTTCCAGGAGCGAGATC; 5′-GCTGTTGTCATACTTCT-CATGG), TMPRSS2 (5′-CCTGACGCAGGCTTCCAAC; 5′-GGTCAAGGTGATGCACAGTG), FKBP5 (5′-GCGAAGGAGAA-GACCACGACAT; 5′-TAGGCTTCCCTGCCTCTCCAAA), and

FOXA1 (5′-GCAATACTCGCCTTACGGCT; 5′-TACA-CACCTTGGTAGTACGCC). Results were normalized to GADPH expression level, and each sample was quantified in triplicate. Relative quantification considers GAPDH internal standard and control conditions (PC3-CNT without DHT) to normalize and compare samples. GraphPad Prism 8.0 software was used to perform the statistical analyses using *t* test, which confirmed the normal distribution of the values.

Proximity ligation assay

PLA experiments were performed using reagents from the Naveniflex MR Kit (Navinci) essentially as previously described (*102*). Briefly, cells were seeded onto coverslips in 12-well plates, fixed in methanol for 2 min, and then washed twice in 1× phosphate-buffered saline. Fixed cells were stored at 4°C for subsequent staining or saturated with the blocking solution for 1 hour at 37°C. All further steps were performed at this temperature. Cells were then incubated with different pairs of primary antibodies: (i) anti-AR (Cell Signaling, #5153) and anti-PRMT5 (Santa Cruz Biotechnology, sc-376937), (ii) anti-AR (Santa Cruz, sc-7305) and anti-MMA (Cell Signaling, #8711), or (iii) anti-AR (Santa Cruz, sc-7305) and anti-SDMA (Cell Signaling, #13222) for 1 hour. After three washes in tris-buffered saline with 0.1% Tween® 20 detergent (TBS-T), mouse and rabbit secondary antibodies conjugated with complementary oligonucleotides ("Navenibodies") were added and incubated for 1 hour. Again, cells were washed three times in TBS-T and subsequently incubated with reaction reagents A, B, and C to activate the oligonucleotides, to allow the interaction of Navenibodies that are in close proximity and the DNA hybridization and amplification of the proximity fluorescent probes (ATTO647), respectively. Last, cells were washed 2 min in 1× tris-buffered saline (TBS) and incubated for 15 min with 0.1× TBS at room temperature. The samples were mounted using Duolink in situ mounting medium containing 4′,6-diamidino-2-phenylindole (DAPI; Sigma-Aldrich, #DUO82040). The edges of the coverslips were sealed using nail polish. Slides were then stored in the dark at 4°C for a short term or visualized under a Zeiss fluorescence microscope, and interactions were counted for at least 300 cells using ImageJ software (*103*). In some experiments, PRMT5 was downregulated using ON-TARGETplus Human SMARTpool small interfering RNA (siRNAs; Dharmacon, #L-015817-00-0005). The unrelated siRNA ON-TARGETplus Non-targeting Control Pool (Dharmacon, #D-001810-10-05) was used as control in these siRNA experiments. Alternatively, PRMT5 activity was blocked by preincubating the cells for 48 hours with the specific inhibitor, GSK595 (0.5 μM; Sigma-Aldrich). Cells incubated with the same volume of dimethyl sulfoxide were used as reference in these experiments.

Cloning and mutagenesis of the hAR-LBD construct

Recombinant human AR-LBD (hAR-LBD; amino acids 641 to 920) was cloned into a modified pGEX vector as previously published (*63*). The resulting fusion protein consists of a histidine tag sequence followed by a glutathione *S*-transferase and a *Tobacco etch* virus (TEV) cleavage site before the corresponding sequence of the hAR-LBD. The pGEX vector template encoding WT hAR-LBD was mutated using the Q5 Site-Directed Mutagenesis Kit (New England Biolabs) to generate AR-LBD mutant vectors with the following primers (Y764C: 5′-CAGGATGCTCTgGCTTCGC, 5′-

GAGTTGACATTGGTGAAGGATCG; V758A: 5′- TTCAC-CAATGcCAACTCCAGGATGCTC, 5′- GGATCGCCAGCC-CATGGC; F755V: 5′- CTGGCGATCCgTCACCAATGT, 5′-CCCATGGCAAACACCATGAGC; F755L: 5′- CTGGCGATCCT-TaACCAATGT, 5′- CCCATGGCAAACACCATGAGC; and Q799E: 5′- TGGATGGCTCgAAATCACCCC, 5′-AACTCTTGAGAGAGGTGC).

Differential scanning fluorimetry

Thermofluor experiments were performed in an iQ5 Multicolor Real-Time PCR Detection System (Bio-Rad) using 96-well plates (Hard-Shell High-Profile Semi-Skirted PCR Plate, Bio-Rad) and a 25-μl total volume for each reaction essentially as described in *104*. Melting curves were acquired from eight replicates to determine the average T_m. AR samples (0.5 mg/ml) were prepared in 20 mM Hepes (pH 8.0), 150 mM Li_2SO_4, 10% glycerol, 50 mM imidazole, 1 mM dithiothreitol (DTT), and 50 μM DHT and centrifuged 5 min at 14,000 rpm. SYPRO Orange dye (Sigma-Aldrich) was first prepared at 80× in the protein buffer, starting from a 5000× commercial dilution. The final concentration of SYPRO Orange dye in each 25-μl reaction was 5×. The plates were sealed with optical quality sealing film (Microseal B Seals, Bio-Rad) and centrifuged at 2000*g* for 30 s. Samples were equilibrated for 60 s and analyzed using a linear gradient from 16° to 95°C in increments of 1°C/min, recording the SYPRO orange fluorescence throughout the gradient in the iQ5 Optical System Software 2.0. Values were fitted using the online tool JTSA with the Boltzmann four-parameter logistic equation, and the calculated fluorescence shift midpoints were compared via unpaired *t* test for equal variances in GraphPad Prism 8.

Proteolytic digestion

Samples of recombinant WT AR-LBD and all studied mutants were buffered-exchanged into 25 mM tris (pH 7.6), 10 mM $CaCl_2$, and 1 mM DTT using a PD-10 column and concentrated to 0.5 mg/ml using a centrifugal filter device. Sequencing-grade Arg-C protease (Clostripain, P5214 Abnova) was added [50/1 (w/w), protein/protease], and mixtures were incubated at 37°C with shaking. Aliquots of the proteolytic reactions were taken at indicated times, immediately mixed with reducing Laemmli buffer, and heated at 95°C for 5 min. Reaction products were separated on SDS-polyacrylamide gels and stained with Coomassie Brilliant Blue.

Crystallization and structure determination

Purified, concentrated DHT-bound AR-LBD mutants (F755L, F755V, V758A, Y764C, and Q799E) were combined with a twofold molar excess of UBA3 peptide and incubated for 1 hour at room temperature. Drops of the AR-LBD mixture were equilibrated against 0.1 M tris-HCl (pH 8.0) containing either 0.2 M sodium chloride, 2.0 M ammonium sulfate, 0.1 M ammonium acetate, or 2.5 M sodium formate using the sitting drop vapor-diffusion method. Diffraction data were collected at 100 K at the XALOC beamline of the ALBA-CELLS synchrotron (www.cells.es/en/beamlines/bl13-xaloc) and processed using MOSFLM (www.mrc-lmb.cam.ac.uk/harry/mosflm/) and CCP4 (www.ccp4.ac.uk/). The crystal structures were solved and refined using MOLREP (www.ccp4.ac.uk/html/molrep.html#references), REFMAC5 (www2.mrc-lmb.cam.ac.uk/groups/murshudov/content/refmac/refmac.html), and COOT (www2.mrc-lmb.cam.ac.

uk/personal/pemsley/coot/) from the CCP4 package. Crystal packing was analyzed using PISA (www.ebi.ac.uk/), model quality was assessed with MolProbity (http://molprobity.biochem.duke.edu/), and structure figures were prepared with PyMOL (www.pymol.org).

Cross-linking experiments
Purified recombinant WT and mutant AR-LBD proteins were incubated with fourfold molar excess of BMOE or BMB cross-linkers for 2 hours at 37°C following the manufacturer's instructions. Samples of the reaction mixtures were boiled in the presence of reducing Laemmli sample buffer and resolved by SDS-PAGE.

Y764C covalent dimerization in solution
Purified recombinant Y764C (3 mg/ml) was incubated in 20 mM Hepes (pH 8.0), 150 mM Li_2SO_4, 10% glycerol, 50 mM imidazole, 1 mM DTT, 50 μM DHT, or in the same buffer without DTT after desalting using a PD-10 column (GE Healthcare). Y764C samples incubated under reducing and nonreducing conditions were boiled in the presence of reducing Laemmli sample buffer and resolved in a 10% SDS-polyacrylamide gel.

Nano–liquid chromatography–MS/MS experiments
Bands corresponding to dimeric, BMB–cross-linked Y764C were excised from the gels and subjected to in-gel digestion following the standard protocols. Briefly, excised bands were reduced (10 mM DTT) in 50 mM bicarbonate buffer (pH 8.0) for 45 min at 56°C, alkylated (50 mM iodoacetamide in 50 mM ammonium bicarbonate buffer for 30 min at 25°C), and digested with trypsin overnight at 37°C in 100 mM ammonium acetate buffer (pH 8). (Sequencing-grade endoproteases were from Promega).

The following procedures have been performed as previously published (64). Tryptic peptides were diluted in 1% formic acid (FA) and loaded onto a 180 μm by 20 mm C18 Symmetry trap column (Waters) at a flow rate of 15 μl/min using a nanoAcquity Ultra Performance LCTM chromatographic system (Waters). Peptides were separated using a C18 analytical column (BEH130 C18, 75 mm by 25 cm, 1.7 μm; Waters) with a 120-min run, comprising three consecutive linear gradients: from 1 to 35% B in 100 min, from 35 to 50% B in 10 min, and from 50 to 85% B in 10 min (A = 0.1% FA in water, B = 0.1% FA in CH_3CN). The column outlet was directly connected to an Advion TriVersa NanoMate fitted on an Linear trap quadrupole furier transform (LTQ-FT) Ultra mass spectrometer (Thermo Fisher Scientific), which was operated in positive mode using the data-dependent acquisition mode. Survey MS scans were acquired in the Fourier transform ion cyclotron resonance (FT-ICR) cell with the resolution (defined at 400 mass/charge ratio) set to 100,000. Up to six of the most intense ions per scan were fragmented and detected in the linear ion trap. The ion count target value was 1,000,000 for the survey scan and 50,000 for the MS/MS scan. Target ions already selected for MS/MS were dynamically excluded for 30 s. Spray voltage in the NanoMate source was set to 1.70 kV. Capillary voltage and tube lens on the LTQ-FT were tuned to 40 and 120 V, respectively. The minimum signal required to trigger MS to MS/MS switch was set to 1000, and activation Q value was set at 0.25. Singly charged precursors were rejected for fragmentation.

Docking experiments and dimeric interface analysis
The dimerization energy of the AR-LBD dimeric conformation found in the x-ray structure (PDB 5JJM, chains B:C) as well as that of the modeled mutant dimers (built by superimposition of the mutant monomeric structures onto the corresponding subunits of the crystallographic dimer) was computed with the pyDock bindEy module (105) based on energy terms previously optimized for rigid-body docking. The pyDock binding energy is basically composed of Lennard-Jones VdW, Coulombic electrostatics, and implicit desolvation based on accessible surface area (ASA) with atomic solvation parameters optimized for protein-protein interactions (106). To avoid excessive penalization from possible clashes derived from the rigid-body approach, VdW total contribution was weighed by a factor of 0.1. For the same reason, VdW and electrostatic values per intermolecular atom pair were restricted to a maximum of +1.0 kcal/mol or to a range between −1.0 and +1.0 kcal/mol, respectively. BSA values of WT and mutant dimers were computed as the difference in ASA between the dimer and the unbound molecules, using ICM-Browser (www.molsoft.com). In addition, homodimeric docking models of WT AR-LBD and its mutants were built using the pyDock docking and scoring method (105). First, protein models were prepared by removing all cofactors and heteroatoms, and missing side chains were modeled with SCWRL 3.0 (105). Then, the fast Fourier transform–based docking programs FTDock (with electrostatics and 0.7 Å grid resolution) (www.sbg.bio.ic.ac.uk/docking/ftdock.html) and ZDOCK 2.1 (https://zdock.umassmed.edu/) were used to generate 10,000 and 2000 rigid-body docking poses, respectively. These were merged in a single pool for subsequent pyDock scoring, as detailed above. From the resulting docking poses, NIP values were obtained for each residue with the built-in patch module of pyDock, implementing the pyDockNIP algorithm (65). An NIP value of 1 indicates that the corresponding residue is involved in all predicted interfaces of the 100 lowest energy docking solutions, while a value of 0 means that it appears as expected by random chance. Last, a negative NIP value implies that the residue appears at the low-energy docking interfaces less often than random. Usually, residues with NIP ≥ 0.2 are considered as hotspot residues. In addition, ODA was obtained by computing surface patches with optimal desolvation energy generated from each surface residue (66). Residues with low ODA values, usually less than −10.0 kcal/mol, indicate regions with favorable desolvation energy upon interaction with a partner protein. Residues from Lys^{845} to Ser^{851} were removed from WT for all energy and docking calculations, for consistency in the comparative analysis, since these residues are missing in all mutant structures. Additional docking experiments were performed using the LZerD protein docking web server (https://lzerd.kiharalab.org/) with the structure of a hetero-tetrameric $(PRMT5)_2$·$(MEP50)_2$ complex as receptor (PDB 7L1G) and the current structure of AR-LBD(Q799E) as ligand. Solutions that satisfied the constraints (distance of Arg^{761}-flanking residues to the PRMNT5 catalytic machinery, <6 Å) were visually inspected.

Computational analysis of the estimated energetic impact of AR point mutations
We estimated the impact of the studied mutations on the overall protein stability with the FoldX empirical force (https://foldxsuite.crg.eu/) (107). Ten iterations were conducted for each mutation and later averaged. Computed free energy differences between mutant

and WT proteins (estimated $\Delta\Delta G$) < 1 kcal/mol were considered not significant, those between 1 and 2, 2 and 4, and >4 kcal/mol as slightly, mildly, and strongly destabilizing, respectively. (FoldX has an estimated error of ~0.7 kcal/mol).

Statistical coupling analysis

Following previously published protocol [(64), DOI: 10.5281/zenodo.7274365], we identified two different sectors by using the SCA5 8/2011 version (108) and the updated version pySCA (109–110) with an alignment of 880 sequences. The stability of the identified sectors was assessed with a statistical test based on hypergeometric calculations of the groups of residues belonging to given sectors between pairs of alignments. P values were adjusted using FDR. Next, specific residues from the significant sectors were extracted and selected according to their rank.

Molecular dynamic simulations
System preparation

The crystal structure of monomeric AR-LDB·DHT (PDB 1T7T) was used to represent the WT receptor, while the x-ray mutant structures used were those determined in this work. In a first step, hydrogens were added to all protein residues in their corresponding protonation states at pH 7.0, and side chain orientations were adjusted using the Protein Preparation Wizard workflow included in Maestro v.10.0 software package (www.schrodinger.com/products/maestro). Missing residues in all the mutant structures (Lys[845] to Ser[851]) were obtained from the WT structure by superposition. The parameters for DHT were obtained using the general amber force field (gaff2) (111), and charges were generated with the restrained electrostatic potential (112) at the HF/6-31G(d,p) level using the Antechamber module of AMBER18 (https://ambermd.org/). Next, each system was placed in a cubic periodic box filled with Optimal Point Charge water molecules (113), setting a minimum distance of 15 Å between the solute and the box walls. Water molecules closer than 1.0 Å to any complex atom were removed. Then, counter ions were added to neutralize the system following a grid-shaped procedure for mapping the electrostatic potential surface. All calculations were done using the ff19SB force field (114) with a cutoff of 10 Å for noncovalent interactions, applying the PME (Particle Mesh Ewald) method (115) for the treatment of the electrostatic interactions.

Molecular dynamics

Before starting the MD calculations, the structures were first relaxed to eliminate possible steric clashes with a 5000-step minimization procedure using the steepest descent method. Then, the systems were stepwise heated to 300 K at a rate of 30 K every 20 ps, fixing the main atoms of the proteins with a harmonic positional restriction of 5 kcal/mol Å^{-2}, using the Langevin thermostat algorithm with a collision frequency of 3 ps^{-1} under the NVT ensemble (heating). Subsequently, 100-ps simulations were performed at constant pressure (NPT ensemble) keeping fixed the main atoms with the same harmonic positional restrictions for density equilibration (density equilibration). Last, conventional MD of 1 μs for all the mutants and 1.2 μs for the WT protein were carried out within the NVT ensemble in quadruplicate to increase the conformational sampling of the system (116). The ParmEd program (https://parmed.github.io/ParmEd/html/index.html) was used to introduce hydrogen mass repartitioning to allow integration times

of 4 fs (117), and the SHAKE algorithm (118) was used to constrain the bonds involving the hydrogen atoms.

RMSD and RMSF

RMSD along the simulation time was computed using the CPPTRAJ module from AMBER18 (https://amber-md.github.io/cpptraj/CPPTRAJ.xhtml) for all the MD trajectories to assess the structural stability of the systems along time. RMSD was computed with respect to all the Cα atoms, using the not minimized x-ray structure of the WT as reference for all the systems. The resulting superimposed trajectories were used to calculate the RMSF for each of the residues of the protein to obtain information about their conformational flexibility.

Residue pair distance

To quantify the effect of the different mutations on the distances between AR residue pairs, we implemented the algorithm described by Vatansever and coworkers (119). This algorithm is based on the concept of first coordination shell defined in the Gaussian network model but extended to a SCS with a radius of ~9.1 Å to better account for the contribution of nonbonded pairs (120). Briefly, for each Cα,i atom, the time-averaged distance to any other Cα,j atom that belongs to its SCS was obtained for the WT ($\overline{R}_{ij,\text{WT}}$) and the studied mutants ($\overline{R}_{ij,\text{mut}}$). Then, the difference ($\Delta\overline{R}_{ij}$) between $\overline{R}_{ij,\text{WT}}$ and $\overline{R}_{ij,\text{mut}}$ was calculated, where $\Delta\overline{R}_{ij} = \overline{R}_{ij,\text{WT}} - \overline{R}_{ij,\text{mut}}$. To this end, we first calculated for all residues the changes in the time-averaged distance between residue i and all j residues that belong to its SCS for the WT structure ($\overline{R}_{ij,\text{WT}}$) and for all mutants ($\overline{R}_{ij,\text{mut}}$). The obtained $\Delta\overline{R}_{ij}$ differences indicate the degree of distortion introduced by a specific mutation. Residue pairs (i and j) that have the largest positive ($\Delta\overline{R}_{ij} > 2.50$ Å) and negative distances ($\Delta\overline{R}_{ij} < -1.40$ Å) between WT and each mutant were highlighted.

Supplementary Materials

This PDF file includes:
Figs. S1 to S6
Tables S1 to S4
References

View/request a protocol for this paper from *Bio-protocol*.

References and Notes

1. W. D. Tilley, C. M. Wilson, M. Marcelli, M. J. McPhaul, Androgen receptor gene expression in human prostate carcinoma cell lines. *Cancer Res.* **17**, 5382–5386 (1990).
2. E. Estébanez-Perpiñá, C. L. Bevan, I. J. McEwan, Eighty years of targeting androgen receptor activity in prostate cancer: The fight goes on. *Cancers* **13**, 509 (2021).
3. A. Jiménez-Panizo, P. Pérez, A. M. Rojas, P. Fuentes-Prior, E. Estébanez-Perpiñá, Non-canonical dimerization of the androgen receptor and other nuclear receptors: Implications for human disease. *Endocr. Relat. Cancer* **26**, R479–R497 (2019).
4. X. Yu, P. Yi, R. A. Hamilton, H. Shen, M. Chen, C. E. Foulds, M. A. Mancini, S. J. Ludtke, Z. Wang, B. W. O'Malley, Structural insights of transcriptionally active, full-length androgen receptor coactivator complexes. *Mol. Cell* **79**, 812–823.e4 (2020).
5. P. L. Shaffer, A. Jivan, D. E. Dollins, F. Claessens, D. T. Gewirth, Structural basis of androgen receptor binding to selective androgen response elements. *Proc. Natl. Acad. Sci. U.S.A.* **101**, 4758–4763 (2004).
6. M. Nadal, S. Prekovic, N. Gallastegui, C. Helsen, M. Abella, K. Zielinska, M. Gay, M. Vilaseca, M. Taulès, A. B. Houtsmuller, M. E. van Royen, F. Claessens, P. Fuentes-Prior, E. Estébanez-Perpiñá, Structure of the homodimeric androgen receptor ligand-binding domain. *Nat. Commun.* **8**, 14388 (2017).

7. E. V. Wasmuth, A. Vanden Broeck, J. R. LaClair, E. A. Hoover, K. E. Lawrence, N. Paknejad, K. Pappas, D. Matthies, B. Wang, W. Feng, P. A. Watson, J. C. Zinder, W. R. Karthaus, M. J. de la Cruz, R. K. Hite, K. Manova-Todorova, Z. Yu, S. T. Weintraub, S. Klinge, C. L. Sawyers, Allosteric interactions prime androgen receptor dimerization and activation. *Mol. Cell.* **82**, 2021–2031 (2022).

8. K. E. Knudsen, T. M. Penning, Partners in crime: Deregulation of AR activity and androgen synthesis in prostate cancer. *Trends Endocrinol. Metab.* **21**, 315–324 (2010).

9. Y. Wen, M. C.-T. Hu, K. Makino, B. Spohn, G. Bartholomeusz, D. H. Yan, M. C. Hung, HER-2/neu promotes androgen-independent survival and growth of prostate cancer cells through the Akt pathway. *Cancer Res.* **60**, 6841–6845 (2000).

10. H. K. Lin, S. Yeh, H. Y. Kang, C. Chang, Akt suppresses androgen-induced apoptosis by phosphorylating and inhibiting androgen receptor. *Proc. Natl. Acad. Sci. U.S.A.* **98**, 7200–7205 (2001).

11. H. K. Lin, Y. C. Hu, L. Yang, S. Altuwaijri, Y. T. Chen, H. Y. Kang, C. Chang, Suppression versus induction of androgen receptor functions by the phosphatidylinositol 3-Kinase/Akt pathway in prostate cancer LNCaP cells with different passage numbers. *J. Biol. Chem.* **278**, 50902–50907 (2003).

12. S. S. Taneja, S. Ha, N. K. Swenson, H. Y. Huang, P. Lee, J. Melamed, E. Shapiro, M. J. Garabedian, S. K. Logan, Cell-specific regulation of androgen receptor phosphorylation in vivo. *J. Biol. Chem.* **280**, 40916–40924 (2005).

13. K. Xu, H. Shimelis, D. E. Linn, R. Jiang, X. Yang, F. Sun, Z. Guo, H. Chen, W. Li, H. Chen, X. Kong, J. Melamed, S. Fang, Z. Xiao, T. D. Veenstra, Y. Qiu, Regulation of androgen receptor transcriptional activity and specificity by RNF6-induced ubiquitination. *Cancer Cell* **15**, 270–282 (2009).

14. D. E. Linn, X. Yang, Y. Xie, A. Alfano, D. Deshmukh, X. Wang, H. Shimelis, H. Chen, W. Li, K. Xu, M. Chen, Y. Qiu, Differential regulation of androgen receptor by PIM-1 kinases via phosphorylation-dependent recruitment of distinct ubiquitin E3 ligases. *J. Biol. Chem.* **287**, 22959–22968 (2012).

15. D. Gioeli, B. M. Paschal, Post-translational modification of the androgen receptor. *Mol. Cell. Endocrinol.* **352**, 70–78 (2012).

16. T. van der Steen, D. J. Tindall, H. Huang, Posttranslational modification of the androgen receptor in prostate cancer. *Int. J. Mol. Sci.* **14**, 14833–14859 (2013).

17. Y. Koryakina, H. Q. Ta, D. Gioeli, Androgen receptor phosphorylation: Biological context and functional consequences. *Endocr. Relat. Cancer* **21**, T131–T145 (2014).

18. Z. Mounir, J. M. Korn, T. Westerling, F. Lin, C. A. Kirby, M. Schirle, G. McAllister, G. Hoffman, N. Ramadan, A. Hartung, Y. Feng, D. R. Kipp, C. Quinn, M. Fodor, J. Baird, M. Schoumacher, R. Meyer, J. Deeds, G. Buchwalter, T. Stams, N. Keen, W. R. Sellers, M. Brown, R. A. Pagliarini, ERG signaling in prostate cancer is driven through PRMT5-dependent methylation of the androgen receptor. *eLife* **5**, e13964 (2016).

19. L. Malbeteau, H. T. Pham, L. Eve, M. R. Stallcup, C. Poulard, M. Le Romancer, How protein methylation regulates steroid receptor function. *Endocr. Rev.* **43**, 160–197 (2022).

20. Q. Wang, W. Li, X. S. Liu, J. S. Carroll, O. A. Jänne, E. K. Keeton, A. M. Chinnaiyan, K. J. Pienta, M. Brown, A hierarchical network of transcription factors governs androgen receptor-dependent prostate cancer growth. *Mol. Cell* **27**, 380–392 (2007).

21. D. Robinson, E. M. Van Allen, Y. M. Wu, N. Schultz, R. J. Lonigro, J. M. Mosquera, B. Montgomery, M. E. Taplin, C. C. Pritchard, G. Attard, H. Beltran, W. Abida, R. K. Bradley, J. Vinson, X. Cao, P. Vats, L. P. Kunju, M. Hussain, F. Y. Feng, S. A. Tomlins, K. A. Cooney, D. C. Smith, C. Brennan, J. Siddiqui, R. Mehra, Y. Chen, D. E. Rathkopf, M. J. Morris, S. B. Solomon, J. C. Durack, V. E. Reuter, A. Gopalan, J. Gao, M. Loda, R. T. Lis, M. Bowden, S. P. Balk, G. Gaviola, C. Sougnez, M. Gupta, E. Y. Yu, E. A. Mostaghel, H. H. Cheng, H. Mulcahy, L. D. True, S. R. Plymate, H. Dvinge, R. Ferraldeschi, P. Flohr, S. Miranda, Z. Zafeiriou, N. Tunariu, J. Mateo, R. Perez-Lopez, F. Demichelis, B. D. Robinson, M. Schiffman, D. M. Nanus, S. T. Tagawa, A. Sigaras, K. W. Eng, O. Elemento, A. Sboner, E. I. Heath, H. I. Scher, K. J. Pienta, P. Kantoff, J. S. De Bono, M. A. Rubin, P. S. Nelson, L. A. Garraway, C. L. Sawyers, A. M. Chinnaiyan, Integrative clinical genomics of advanced prostate cancer. *Cell* **161**, 1215–1228 (2015).

22. D. A. Quigley, H. X. Dang, S. G. Zhao, P. Lloyd, R. Aggarwal, J. J. Alumkal, A. Foye, V. Kothari, M. D. Perry, A. M. Bailey, D. Playdle, T. J. Barnard, L. Zhang, J. Zhang, J. F. Youngren, M. P. Cieslik, A. Parolia, T. M. Beer, G. Thomas, K. N. Chi, M. Gleave, N. A. Lack, A. Zoubeidi, R. E. Reiter, M. B. Rettig, O. Witte, C. J. Ryan, L. Fong, W. Kim, T. Friedlander, J. Chou, H. Li, R. Das, H. Li, R. Moussavi-Baygi, H. Goodarzi, L. A. Gilbert, P. N. Lara, C. P. Evans, T. C. Goldstein, J. M. Stuart, S. A. Tomlins, D. E. Spratt, R. K. Cheetham, D. T. Cheng, K. Farh, J. S. Gehring, J. Hakenberg, A. Liao, P. G. Febbo, Genomic hallmarks and structural variation in metastatic prostate cancer. *Cell* **174**, 758–769.e9 (2018).

23. D. B. Lubahn, T. R. Brown, J. A. Simental, H. N. Higgs, C. J. Migeon, E. M. Wilson, F. S. French, Sequence of the intron/exon junctions of the coding region of the human androgen receptor gene and identification of a point mutation in a family with complete androgen insensitivity. *Proc. Natl. Acad. Sci. U.S.A.* **86**, 9534–9538 (1989).

24. O. Hiort, G. H. Sinnecker, P. M. Holterhus, E. M. Nitsche, K. Kruse, The clinical and molecular spectrum of androgen insensitivity syndromes. *Am. J. Med. Genet.* **63**, 218–222 (1996).

25. I. A. Hughes, J. D. Davies, T. I. Bunch, V. Pasterski, K. Mastroyannopoulou, J. Macdougall, Androgen insensitivity syndrome. *Lancet* **380**, 1419–1428 (2012).

26. C. E. Bohl, W. Gao, D. D. Miller, C. E. Bell, J. T. Dalton, Structural basis for antagonism and resistance of bicalutamide in prostate cancer. *Proc. Natl. Acad. Sci. U.S.A.* **102**, 6201–6206 (2005).

27. C. E. Bohl, Z. Wu, D. D. Miller, C. E. Bell, J. T. Dalton, Crystal structure of the T877A human androgen receptor ligand-binding domain complexed to cyproterone acetate provides insight for ligand-induced conformational changes and structure-based drug design. *J. Biol. Chem.* **282**, 13648–13655 (2007).

28. J. S. Sack, K. F. Kish, C. Wang, R. M. Attar, S. E. Kiefer, Y. An, G. Y. Wu, J. E. Scheffler, M. E. Salvati, R. Krystek, R. Weinmann, H. M. Einspahr, Crystallographic structures of the ligand-binding domains of the androgen receptor and its T877A mutant complexed with the natural agonist dihydrotestosterone. *Proc. Natl. Acad. Sci. U.S.A.* **98**, 4904–4909 (2001).

29. B. Gottlieb, L. K. Beitel, A. Nadarajah, M. Paliouras, M. Trifiro, The androgen receptor gene mutations database: 2012 update. *Hum. Mutat.* **33**, 887–894 (2012).

30. Z. Culig, A. Hobisch, M. Erdel, G. Bartsch, H. Klocker, Studies on androgen receptor mutations and amplification in human prostate cancer. *Methods Mol. Med.* **81**, 267–275 (2003).

31. E. R. Hyytinen, K. Haapala, J. Thompson, I. Lappalainen, M. Roiha, I. Rantala, H. J. Helin, O. A. Jänne, M. Vihinen, J. J. Palvimo, P. A. Koivisto, Pattern of somatic androgen receptor gene mutations in patients with hormone-refractory prostate cancer. *Lab. Invest.* **82**, 1591–1598 (2002).

32. M. J. McPhaul, M. Marcelli, S. Zoppi, C. M. Wilson, J. E. Griffin, J. D. Wilson, Mutations in the ligand-binding domain of theandrogen receptor gene cluster in two regions of the gene. *J. Clin. Invest.* **90**, 2097–2101 (1992).

33. C. Radmayr, Z. Culig, A. Hobisch, S. Corvin, G. Bartsch, H. Klocker, Analysis of a mutant androgen receptor offers a treatment modality in a patient with partial androgen insensitivity syndrome. *Eur. Urol.* **33**, 222–226 (1998).

34. T. R. Brown, D. B. Lubahn, E. M. Wilson, F. S. French, C. J. Migeon, J. L. Corden, Functional characterization of naturally occurring mutant androgen receptors from subjects with complete androgen insensitivity. *Mol. Endocrinol.* **4**, 1759–1772 (1990).

35. J. M. Lobaccaro, S. Lumbroso, R. Ktari, R. Dumas, C. Sultan, An exonic point mutation creates a MaeIII site in the androgen receptor gene of a family with complete androgen insensitivity syndrome. *Hum. Mol. Genet.* **2**, 1041–1043 (1993).

36. Y.-H. Liu, C. Li, S.-F. Zhou, Prediction of deleterious functional effects of non-synonymous single nucleotide polymorphisms in human nuclear receptor genes using a bioinformatics approach. *Drug Metab. Lett.* **3**, 242–286 (2009).

37. R. Tadokoro-Cuccaro, T. I. Bunch, J. W. Schwabe, I. A. Hughes, J. C. Murphy, Comparison of the molecular consequences of different mutations at residue 754 and 690 of the androgen receptor (AR) and androgen insensitivity syndrome (AIS) phenotype. *Clin. Endocrinol.* **71**, 253–260 (2009).

38. M. Marcelli, M. Ittmann, S. Mariani, R. Sutherland, R. Nigam, L. Murthy, Y. Zhao, D. Diconcini, E. Puxeddu, A. Esen, J. Eastham, N. L. Weigel, D. J. Lamb, Androgen receptor mutations in prostate cancer. *Cancer Res.* **60**, 944–949 (2000).

39. X. B. Shi, A. H. Ma, L. Xia, H. J. Kung, R. W. De Vere White, Functional analysis of 44 mutant androgen receptors from human prostate cancer. *Cancer Res.* **62**, 1496–1502 (2002).

40. X. E. Zhou, K. M. Suino-Powell, J. Li, Y. He, J. P. MacKeigan, K. Melcher, E. L. Yong, H. E. Xu, Identification of SRC3/AIB1 as a preferred coactivator for hormone-activated androgen receptor. *J. Biol. Chem.* **285**, 9161–9171 (2010).

41. S. Grosdidier, L. R. Carbó, V. Buzón, G. Brooke, P. Nguyen, J. D. Baxter, C. L. Bevan, P. Webb, E. Estébanez-Perpiñá, J. Fernández-Recio, Allosteric conversation in the androgen receptor ligand-binding domain surfaces. *Mol. Endocrinol.* **26**, 1078–1090 (2012).

42. C. W. Hay, I. J. McEwan, The impact of point mutations in the human androgen receptor: Classification of mutations on the basis of transcriptional activity. *PLOS ONE* **7**, e32514 (2012).

43. M. J. McPhaul, M. Marcelli, W. D. Tilley, J. E. Griffin, R. F. Isidro-Gutierrez, J. D. Wilson, Molecular basis of androgen resistance in a family with a qualitative abnormality of the androgen receptor and responsive to high-dose androgen therapy. *J. Clin. Invest.* **87**, 1413–1421 (1991).

44. I. Murono, B. B. Mendonca, I. J. Arnhold, A. C. Rigon, C. J. Migeon, T. R. Brown, Human androgen insensitivity due to point mutations encoding amino acid substitutions in the androgen receptor steroid-binding domain. *Hum. Mutat.* **6**, 152–162 (1995).

45. C. A. Quigley, A. De Bellis, K. B. Marschke, M. K. El-Awady, E. M. Wilson, F. S. French, Androgen receptor defects: Historical, clinical, and molecular perspectives. *Endocr. Rev.* **16**, 271–321 (1995).

46. E. Langley, J. A. Kemppainen, E. M. Wilson, Intermolecular NH2–/carboxyl-terminal interactions in androgen receptor dimerization revealed by mutations that cause androgen insensitivity. *J. Biol. Chem.* **273**, 92–101 (1998).

47. K. F. Melo, B. B. Mendonca, A. E. C. Billerbeck, E. M. Costa, M. Inácio, F. A. Silva, A. M. Leal, A. C. Latronico, I. J. Arnhold, Clinical, hormonal, behavioral, and genetic characteristics of androgen insensitivity syndrome in a Brazilian cohort: Five novel mutations in the androgen receptor gene. *J. Clin. Endocrinol. Metab.* **88**, 3241–3250 (2003).

48. I. Jääskeläinen, A. Deeb, J. W. Schwabe, N. P. Mongan, H. Martin, I. A. Hughes, Human androgen receptor gene ligand-binding-domain mutations leading to disrupted interaction between the N- and C-terminal domains. *J. Mol. Endocrinol.* **36**, 361–368 (2006).

49. J. Batch, D. Williams, H. Davies, B. Brown, B. A. Evans, I. A. Hughes, M. Patterson, Androgen receptor gene mutations identified by SSCP in fourteen subjects with androgen insensitivity syndrome. *Hum. Mol. Genet.* **1**, 497–503 (1992).

50. C. L. Bevan, B. B. Brown, H. R. Davies, B. A. Evans, I. A. Hughes, M. N. Patterson, Functional analysis of six androgen receptor mutations identified in patients with partial androgen insensitivity syndrome. *Hum. Mol. Genet.* **5**, 265–273 (1996).

51. Q. Wang, F. J. Ghadessy, A. Trounson, D. de Kretser, R. McLachlan, S. Ng, E. Yong, Azoospermia associated with a mutation in the ligand-binding domain of an androgen receptor displaying normal ligand binding, but defective trans-activation. *J. Clin. Endocrinol. Metab.* **83**, 4303–4309 (1998).

52. O. Hiort, P.-M. Holterhus, T. Horter, W. Schulze, B. Kremke, M. Bals-Pratsch, G. H. G. Sinnecker, K. Kruse, Significance of Mutations in the Androgen Receptor Gene in Males with Idiopathic infertility. *J. Clin. Endocrinol. Metab.* **85**, 2810–2815 (2000).

53. N. Kalfa, P. Philibert, R. Werner, F. Audran, A. Bashamboo, H. Lehors, M. Haddad, J. M. Guys, R. Reynaud, P. Alessandrini, K. Wagner, J. Y. Kurzenne, F. Bastiani, J. Bréaud, J. S. Valla, G. M. Lacombe, M. Orsini, J. P. Daures, O. Hiort, F. Paris, K. McElreavey, C. Sultan, Minor hypospadias: The "Tip of the Iceberg" of the partial androgen insensitivity syndrome. *PLOS ONE* **8**, e61824 (2013).

54. J. Qi, M. Tripathi, R. Mishra, N. Sahgal, L. Fazil, S. Ettinger, W. J. Placzek, G. Claps, L. W. Chung, D. Bowtell, M. Gleave, N. Bhowmick, Z. A. Ronai, The E3 ubiquitin ligase siah2 contributes to castration-resistant prostate cancer by regulation of androgen receptor transcriptional activity. *Cancer Cell* **23**, 332–346 (2013).

55. R. Kumar, J. Mendonca, O. Owoyemi, K. Boyapati, N. Thomas, S. Kanacharoen, M. Coffey, D. Topiwala, C. Gomes, B. Ozbek, T. Jones, M. Rosen, L. Dong, S. Wiens, W. N. Brennen, J. T. Isaacs, A. M. D. Marzo, M. C. Markowski, J. C. Zhang, K. J. Pienta, D. M. Pardoll, M. A. Carducci, S. R. Denmeade, S. K. Kachhap, Supraphysiologic testosterone induces ferroptosis and activates immune pathways through nucleophagy in prostate cancer. *Cancer Res.* **81**, 5948–5962 (2021).

56. H. M. Lam, H. M. Nguyen, M. P. Labrecque, L. G. Brown, I. M. Coleman, R. Gulati, B. Lakely, D. Sondheim, P. Chatterjee, B. T. Marck, A. M. Matsumoto, E. A. Mostaghel, M. T. Schweizer, P. S. Nelson, E. Corey, Durable response of enzalutamide-resistant prostate cancer to supraphysiological testosterone is associated with a multifaceted growth suppression and impaired DNA damage response transcriptomic program in patient-derived xenografts. *Eur. Urol.* **77**, 144–155 (2020).

57. L. Garcia-Alonso, C. H. Holland, M. M. Ibrahim, D. Turei, J. Saez-Rodriguez, Benchmark and integration of resources for the estimation of human transcription factor activities. *Genome Res.* **29**, 1363–1375 (2019).

58. A. Aytes, A. Mitrofanova, C. Lefebvre, M. J. Alvarez, M. Castillo-Martin, T. Zheng, J. A. Eastham, A. Gopalan, K. J. Pienta, M. M. Shen, C. Califano, C. Abate-Shen, Cross-species regulatory Network Analysis identifies a synergistic interaction between FOXM1 and CENPF that drives prostate cancer malignancy. *Cancer Cell* **25**, 638–651 (2014).

59. H. Takahashi, M. Furusato, W. C. Allsbrook, H. Nishii, S. Wakui, J. C. Barrett, J. Boyd, Prevalence of androgen receptor gene mutations in latent prostatic carcinomas from japanese men. *Cancer Res.* **55**, 1621–1624 (1995).

60. W. Weidemann, B. Linck, H. Haupt, B. Mentrup, G. Romalo, K. Stockklauser, A. O. Brinkmann, H. U. Schweikert, K. D. Spindler, Clinical and biochemical investigations and molecular analysis of subjects with mutations in the androgen receptor gene. *Clin. Endocrinol.* **45**, 733–739 (1996).

61. J. Thompson, F. Saatcioglu, O. A. Jänne, J. J. Palvimo, Disrupted amino- and carboxyl-terminal interactions of the androgen receptor are linked to androgen insensitivity. *Mol. Endocrinol.* **15**, 923–935 (2001).

62. O. A. O'Mahony, M. P. Steinkamp, M. A. Albertelli, M. Brogley, H. Rehman, D. M. Robins, Profiling human androgen receptor mutations reveals treatment effects in a mouse model of prostate cancer. *Mol. Cancer Res.* **6**, 1691–1701 (2008).

63. E. Estébanez-Perpiñá, L. A. Arnold, P. Nguyen, E. D. Rodrigues, E. Mar, R. Bateman, P. Pallai, K. M. Shokat, J. D. Baxter, R. K. Guy, P. Webb, R. J. Fletterick, A surface on the androgen receptor that allosterically regulates coactivator binding. *Proc. Natl. Acad. Sci. U.S.A.* **104**, 16074–16079 (2007).

64. A. Jiménez-Panizo, A. Alegre-Martí, T. T. Tettey, G. Fettweis, M. Abella, R. Antón, T. A. Johnson, S. Kim, R. L. Schiltz, I. Núñez-Barrios, J. Font-Díaz, C. Caelles, A. F. Valledor, P. Pérez, A. M. Rojas, J. Fernández-Recio, D. M. Presman, G. L. Hager, P. Fuentes-Prior, E. Estébanez-Perpiñá, The multivalency of the glucocorticoid receptor ligand-binding

65. S. Grosdidier, J. Fernández-Recio, Identification of hot-spot residues in protein-protein interactions by computational docking. *BMC Bioinformatics* **9**, 447 (2008).

66. J. Fernandez-Recio, M. Totrov, C. Skorodumov, R. Abagyan, Optimal docking area: A new method for predicting protein-protein interaction sites. *Proteins* **58**, 134–143 (2005).

67. L. Sun, M. Wang, Z. Lv, N. Yang, Y. Liu, S. Bao, W. Gong, R. M. Xu, Structural insights into protein arginine symmetric dimethylation by PRMT5. *Proc. Natl. Acad. Sci. U.S.A.* **108**, 20538–20543 (2011).

68. S. Antonysamy, Z. Bonday, R. M. Campbell, B. Doyle, Z. Druzina, T. Gheyi, B. Han, L. N. Jungheim, Y. Qian, C. Rauch, M. Russell, J. M. Sauder, S. R. Wasserman, K. Weichert, F. S. Willard, A. Zhang, S. Emtage, Crystal structure of the human PRMT5:MEP50 complex. *Proc. Natl. Acad. Sci. U.S.A.* **109**, 17960–17965 (2012).

69. M. C. Ho, C. Wilczek, J. B. Bonanno, L. Xing, J. Seznec, T. Matsui, L. G. Carter, T. Onikubo, P. R. Kumar, M. K. Chan, M. Brenowitz, R. H. Cheng, U. Reimer, S. C. Almo, D. Shechter, Structure of the arginine methyltransferase PRMT5-MEP50 reveals a mechanism for substrate specificity. *PLOS ONE* **8**, e57008 (2013).

70. K. M. Mulvaney, C. Blomquist, N. Acharya, R. Li, M. J. Ranaghan, M. O'Keefe, D. J. Rodriguez, M. J. Young, D. Kesar, D. Pal, M. Stokes, A. J. Nelson, S. S. Jain, A. Yang, Z. Mullin-Bernstein, J. Columbus, F. K. Bozal, A. Skepner, D. Raymond, S. LaRussa, D. C. McKinney, Y. Freyzon, Y. Baidi, D. Porter, A. J. Aguirre, A. Ianari, B. McMillan, W. R. Sellers, Molecular basis for substrate recruitment to the PRMT5 methylosome. *Mol. Cell* **81**, 3481–3495.e7 (2021).

71. M. T. Schweizer, E. S. Antonarakis, H. Wang, A. Seun Ajiboye, A. Spitz, H. Cao, J. Luo, M. C. Haffner, S. Yegnasubramanian, M. A. Carducci, M. A. Eisenberger, J. T. Isaacs, S. R. Denmeade, Effect of bipolar androgen therapy for asymptomatic men with castration-resistant prostate cancer: Results from a pilot clinical study. *Sci. Transl. Med.* **7**, 269ra2 (2015).

72. M. D. Nyquist, L. S. Ang, A. Corella, I. M. Coleman, M. P. Meers, A. J. Christiani, C. Pierce, D. H. Janssens, H. E. Meade, A. Bose, L. Brady, T. Howard, N. De Sarkar, S. B. Frank, R. F. Dumpit, J. T. Dalton, E. Corey, S. R. Plymate, M. C. Haffner, E. A. Mostaghel, P. S. Nelson, Selective androgen receptor modulators activate the canonical prostate cancer androgen receptor program and repress cancer growth. *J. Clin. Invest.* **131**, e146777 (2021).

73. X. Qiu, L. G. Brown, J. L. Conner, H. M. Nguyen, N. Boufaied, S. A. Alaiwi, J. H. Seo, T. El Zarif, C. Bell, E. O'Connor, B. Hanratty, M. Pomerantz, M. L. Freedman, M. Brown, M. C. Haffner, P. S. Nelson, F. Y. Feng, D. P. Labbé, H. W. Long, E. Corey, Response to supraphysiological testosterone is predicted by a distinct androgen receptor cistrome. *JCI Insight* **7**, e157164 (2022).

74. V. Sheikhhassani, B. Scalvini, J. Ng, L. W. H. J. Heling, Y. Ayache, T. M. J. Evers, E. Estébanez-Perpiñá, I. J. McEwan, A. Mashaghi, Topological dynamics of an intrinsically disordered N-terminal domain of the human androgen receptor. *Protein Sci.* **31**, e4334 (2022).

75. S. A. Mosure, P. Munoz-Tello, K.-T. Kuo, B. M. Tavish, X. Yu, D. Scholl, C. C. Williams, T. S. Strutzenberg, J. Bass, R. Brust, A. A. Deniz, P. R. Griffin, D. J. Kojetin, Structural basis of interdomain communication in PPARγ (2022); www.biorxiv.org/content/10.1101/2022.07.13.499031v1.abstract.

76. X. Zhang, X. Cheng, Structure of the predominant protein arginine methyltransferase PRMT1 and analysis of its binding to substrate Peptides. *Structure* **11**, 509–520 (2003).

77. D. Musiani, J. Bok, E. Massignani, L. Wu, T. Tabaglio, M. R. Ippolito, A. Cuomo, U. Ozbek, H. Zorgati, U. Ghoshdastider, R. C. Robinson, E. Guccione, T. Bonaldi, Proteomics profiling of arginine methylation defines PRMT5 substrate specificity. *Sci. Signal.* **12**, eaat8388 (2019).

78. E. S. Burgos, C. Wilczek, T. Onikubo, J. B. Bonanno, J. Jansong, U. Reimer, D. Shechter, Histone H2A and H4 N-terminal tails are positioned by the MEP50 WD repeat protein for efficient methylation by the PRMT5 arginine methyltransferase. *J. Biol. Chem.* **290**, 9674–9689 (2015).

79. P. Chymkowitch, N. Le May, P. Charneau, E. Compe, J. M. Egly, The phosphorylation of the androgen receptor by TFIIH directs the ubiquitin/proteasome process. *EMBO J.* **30**, 468–479 (2011).

80. S. Sarkar, D. L. Brautigan, S. J. Parsons, J. M. Larner, Androgen receptor degradation by the E3 ligase CHIP modulates mitotic arrest in prostate cancer cells. *Oncogene* **33**, 26–33 (2014).

81. C. Liu, W. Lou, J. C. Yang, L. Liu, C. M. Armstrong, A. P. Lombard, R. Zhao, O. D. V. Noel, C. G. Tepper, H. W. Chen, M. Dall'Era, C. P. Evans, A. C. Gao, Proteostasis by STUB1/HSP70 complex controls sensitivity to androgen receptor targeted therapy in advanced prostate cancer. *Nat. Commun.* **9**, 4700 (2018).

82. M. L. Mohler, A. Sikdar, S. Ponnusamy, D. J. Hwang, Y. He, D. D. Miller, R. Narayanan, An overview of next-generation androgen receptor-targeted therapeutics in development for the treatment of prostate cancer. *Int. J. Mol. Sci.* **22**, 2124 (2021).

83. S. Ha, G. Luo, H. Xiang, A comprehensive overview of small-molecule androgen receptor degraders: Recent progress and future perspectives. *J. Med. Chem.* **65**, 16128–16154 (2022).

84. X. Deng, G. Shao, H. T. Zhang, C. Li, D. Zhang, L. Cheng, B. D. Elzey, R. Pili, T. L. Ratliff, J. Huang, C. D. Hu, Protein arginine methyltransferase 5 functions as an epigenetic activator of the androgen receptor to promote prostate cancer cell growth. *Oncogene* **36**, 1223–1231 (2017).

85. K. Hosohata, P. Li, Y. Hosohata, J. Qin, R. G. Roeder, Z. Wang, Purification and identification of a novel complex which is involved in androgen receptor-dependent transcription. *Mol. Cell. Biol.* **23**, 7019–7029 (2003).

86. Y. Peng, F. Chen, J. Melamed, L. Chiriboga, J. Wei, X. Kong, M. Mcleod, Y. Li, C. X. Li, A. Feng, M. J. Garabedian, Z. Wang, R. G. Roeder, P. Lee, Distinct nuclear and cytoplasmic functions of androgen receptor cofactor p44 and association with androgen-independent prostate cancer. *Proc. Natl. Acad. Sci. U.S.A.* **105**, 5236–5241 (2008).

87. L. Zhou, H. Wu, P. Lee, Z. Wang, Roles of the androgen receptor cofactor p44 in the growth of prostate epithelial cells. *J. Mol. Endocrinol.* **37**, 283–300 (2006).

88. S. Yin, L. Liu, C. Brobbey, V. Palanisamy, LE. Ball, S. K. Olsen, M. C. Ostrowski, W. Gan, PRMT5-mediated arginine methylation activates AKT kinase to govern tumorigenesis. *Nat. Commun* **12**, 1–13 (2021).

89. C. Helsen, T. Nguyen, T. Vercruysse, S. Wouters, D. Daelemans, A. Voet, F. Claessens, The T850D phosphomimetic mutation in the androgen receptor ligand binding domain enhances recruitment at activation function 2. *Int. J. Mol. Sci.* **23**, 1557 (2022).

90. I. Maksimovic, Y. David, Non-enzymatic covalent modifications as a new chapter in the histone code. *Trends Biochem. Sci.* **46**, 718–730 (2021).

91. H. S. Soifer, N. Souleimanian, S. Wu, A. M. Voskresenskiy, F. K. Collak, B. Cinar, C. A. Stein, Direct regulation of androgen receptor activity by potent CYP17 inhibitors in prostate cancer cells. *J. Biol. Chem.* **287**, 3777–3787 (2012).

92. A. Dobin, C. A. Davis, F. Schlesinger, J. Drenkow, C. Zaleski, S. Jha, P. Batut, M. Chaisson, T. R. Gingeras, STAR: Ultrafast universal RNA-seq aligner. *Bioinformatics* **29**, 15–21 (2013).

93. A. Frankish, M. Diekhans, A. M. Ferreira, R. Johnson, I. Jungreis, J. Loveland, J. M. Mudge, C. Sisu, J. Wright, J. Armstrong, I. Barnes, A. Berry, A. Bignell, S. Carbonell Sala, J. Chrast, F. Cunningham, T. Di Domenico, S. Donaldson, I. T. Fiddes, C. García Girón, J. M. Gonzalez, T. Grego, M. Hardy, T. Hourlier, T. Hunt, O. G. Izuogu, J. Lagarde, F. J. Martin, L. Martínez, S. Mohanan, P. Muir, F. C. P. Navarro, A. Parker, B. Pei, F. Pozo, M. Ruffier, B. M. Schmitt, E. Stapleton, M. M. Suner, I. Sycheva, B. Uszczynska-Ratajczak, J. Xu, A. Yates, D. Zerbino, Y. Zhang, B. Aken, J. S. Choudhary, M. Gerstein, R. Guigó, T. J. P. Hubbard, M. Kellis, B. Paten, A. Reymond, M. L. Tress, P. Flicek, GENCODE reference annotation for the human and mouse genomes. *Nucleic Acids Res.* **47**, D766–D773 (2019).

94. V. Jimenez-Jacinto, A. Sanchez-Flores, L. Vega-Alvarado, Integrative differential expression analysis for multiple experiments (IDEAMEX): a web server tool for integrated RNA-seq data analysis. *Front. Genet.* **10**, 279 (2019).

95. M. I. Love, W. Huber, S. Anders, Moderated estimation of fold change and dispersion for RNA-seq data with DESeq2. *Genome Biol.* **15**, 550 (2014).

96. M. E. Ritchie, B. Phipson, D. Wu, Y. Hu, C. W. Law, W. Shi, G. K. Smyth, *limma* powers differential expression analyses for RNA-sequencing and microarray studies. *Nucleic Acids Res.* **43**, e47 (2015).

97. Z. Gu, R. Eils, M. Schlesner, Complex heatmaps reveal patterns and correlations in multidimensional genomic data. *Bioinformatics* **32**, 2847–2849 (2016).

98. S. Anders, W. Huber, Differential expression analysis for sequence count data. *Genome Biol.* **11**, R106 (2010).

99. A. Subramanian, P. Tamayo, V. K. Mootha, S. Mukherjee, B. L. Ebert, M. A. Gillette, A. Paulovich, S. L. Pomeroy, T. R. Golub, E. S. Lander, J. P. Mesirov, Gene set enrichment analysis: A knowledge-based approach for interpreting genome-wide expression profiles. *Proc. Natl. Acad. Sci. U.S.A.* **102**, 15545–15550 (2005).

100. T. Wu, E. Hu, S. Xu, M. Chen, P. Guo, Z. Dai, T. Feng, L. Zhou, W. Tang, L. Zhan, X. Fu, S. Liu, X. Bo, G. Yu, clusterProfiler 4.0: A universal enrichment tool for interpreting omics data. *Innovation* **2**, 100141 (2021).

101. M. Schubert, B. Klinger, M. Klünemann, A. Sieber, F. Uhlitz, S. Sauer, M. J. Garnett, N. Blüthgen, J. Saez-Rodriguez, Perturbation-response genes reveal signaling footprints in cancer gene expression. *Nat. Commun.* **9**, 20 (2018).

102. C. Poulard, J. Jacquemetton, T. H. Pham, M. Le Romancer, Using proximity ligation assay to detect protein arginine methylation. *Methods* **175**, 66–71 (2020).

103. J. Schindelin, I. Arganda-Carreras, E. Frise, V. Kaynig, M. Longair, T. Pietzsch, S. Preibisch, C. Rueden, S. Saalfeld, B. Schmid, J. Y. Tinevez, D. J. White, V. Hartenstein, K. Eliceiri, P. Tomancak, A. Cardona, Fiji: An open-source platform for biological-image analysis. *Nat. Methods* **9**, 676–682 (2012).

104. R. Gustafsson, U. Eckhard, W. Ye, E. D. Enbody, M. Pettersson, P. Jemth, L. Andersson, M. Selmer, Structure and characterization of phosphoglucomutase 5 from atlantic and baltic herring—An inactive enzyme with intact substrate binding. *Biomolecules* **10**, 1631 (2020).

105. T. M. K. Cheng, T. L. Blundell, J. Fernandez-Recio, PyDock: Electrostatics and desolvation for effective scoring of rigid-body protein-protein docking. *Proteins Struct. Funct. Genet.* **68**, 503–515 (2007).

106. J. Fernández-Recio, M. Totrov, R. Abagyan, Identification of protein-protein interaction sites from docking energy landscapes. *J. Mol. Biol.* **335**, 843–865 (2004).

107. R. Guerois, J. E. Nielsen, L. Serrano, Predicting changes in the stability of proteins and protein complexes: A study of more than 1000 mutations. *J. Mol. Biol.* **320**, 369–387 (2002).

108. N. Halabi, O. Rivoire, S. Leibler, R. Ranganathan, Protein sectors: evolutionary units of three-dimensional structure. *Cell* **138**, 774–786 (2009).

109. S. W. Lockless, R. Ranganathan, Evolutionarily conserved pathways of energetic connectivity in protein families. *Science* **286**, 295–299 (1999).

110. O. Rivoire, K. A. Reynolds, R. Ranganathan, Evolution-based functional decomposition of proteins. *PLOS Comput. Biol.* **12**, e1004817 (2016).

111. J. Wang, R. M. Wolf, J. W. Caldwell, P. A. Kollman, D. A. Case, Development and testing of a general Amber force field. *J. Comput. Chem.* **25**, 1157–1174 (2004).

112. C. I. Bayly, P. Cieplak, W. D. Cornell, P. A. Kollman, A well-behaved electrostatic potential based method using charge restraints for deriving atomic charges: The RESP model. *J. Phys. Chem.* **97**, 10269–10280 (1993).

113. S. Izadi, R. Anandakrishnan, A. V. Onufriev, Building water models: A different approach. *J. Phys. Chem. Lett.* **5**, 3863–3871 (2014).

114. C. Tian, K. Kasavajhala, K. A. A. Belfon, L. Raguette, H. Huang, A. N. Migues, J. Bickel, Y. Wang, J. Pincay, Q. Wu, C. Simmerling, Ff19SB: Amino-acid-specific protein backbone parameters trained against quantum mechanics energy surfaces in solution. *J. Chem. Theory Comput.* **16**, 528–552 (2020).

115. T. Darden, D. York, L. Pedersen, Particle mesh Ewald: An $N \cdot \log(N)$ method for Ewald sums in large systems. *J. Chem. Phys.* **98**, 10089–10092 (1993).

116. J. J. Perez, M. S. Tomas, J. Rubio-Martinez, Assessment of the sampling performance of multiple-copy dynamics versus a unique trajectory. *J. Chem. Inf. Model.* **56**, 1950–1962 (2016).

117. C. W. Hopkins, S. Le Grand, R. C. Walker, A. E. Roitberg, Long-time-step molecular dynamics through hydrogen mass repartitioning. *J. Chem. Theory Comput.* **11**, 1864–1874 (2015).

118. J. P. Ryckaert, G. Ciccotti, H. J. C. Berendsen, Numerical integration of the cartesian equations of motion of a system with constraints: Molecular dynamics of n-alkanes. *J. Comput. Phys.* **23**, 327–341 (1977).

119. S. Vatansever, B. Erman, Z. H. Gümüş, Oncogenic G12D mutation alters local conformations and dynamics of K-Ras. *Sci. Rep.* **9**, 11730 (2019).

120. A. R. Atilgan, P. Akan, C. Baysal, Small-world communication of residues and significance for protein dynamics. *Biophys. J.* **86**, 85–91 (2004).

121. Y. C. Yang, C. A. Banuelos, N. R. Mawji, J. Wang, M. Kato, S. Haile, I. J. McEwan, S. Plymate, M. D. Sadar, Targeting androgen receptor activation function-1 with EPI to overcome resistance mechanisms in castration-resistant prostate cancer. *Clin. Cancer Res.* **22**, 4466–4477 (2016).

122. N. G. R. D. Elshan, M. B. Rettig, M. E. Jung, Molecules targeting the androgen receptor (AR) signaling axis beyond the AR-Ligand binding domain. *Med. Res. Rev.* **39**, 910–960 (2019).